



Catalytic diversity conferred by confinement of protons within porous aluminosilicates in Prins condensation reactions



Shuai Wang, Enrique Iglesia*

Department of Chemical and Biomolecular Engineering, University of California at Berkeley, Berkeley, CA 94720, USA

ARTICLE INFO

Article history:

Received 11 April 2017

Revised 4 June 2017

Accepted 8 June 2017

Keywords:

Prins condensation

Oligomerization

Isobutanol

Isobutene

2,5-Dimethyl-hexadiene

1,4-Dimethyl-cyclohexene

p-Xylene

Aluminosilicates

Confinement

Density functional theory

ABSTRACT

The effects of confinement of transition states and bound intermediates are described here based on kinetic and theoretical studies for Prins condensation and oligomerization reactions of isobutanol-isobutene reactant mixtures catalyzed by Brønsted acid sites of similar strength but confined within diverse microporous (TON, BEA, MFI, FAU) and mesoporous (Al-MCM-41) aluminosilicate structures. Kinetic data and density functional theory (DFT) show that smaller voids lead to more stable bound monomers derived from isobutene and isobutanol and to protons nearly saturated with H-bonded isobutanol. Prins condensation forms 2,5-dimethyl-hexadiene regioisomers (2,5-DMH) with rate constants that reflect the different stability of the kinetically-relevant C–C bond formation transition states and their H-bonded isobutanol precursors. Their differences in size lead to reactivities that depend sensitively on the size and shape of the confining voids in each aluminosilicate and even on the location of the Al-atoms (and the protons) within a given framework. Specifically, FAU leads to the highest turnover rates, because larger voids in Al-MCM-41 form less effective van der Waals contacts with the transition state, while the smaller voids within TON and BEA lead to enthalpic and entropic penalties brought forth by host-guest distortions. MFI cage-like intersections provide more effective stabilization than BEA cylindrical channels of similar size and lead to higher turnover rates and smaller DFT-derived activation free energies; these subtle effects of void shape on reactivity are neglected in descriptions of the confining frameworks based on spherical constructs. Reactivity descriptors require instead theoretical treatments that rigorously account for van der Waals interactions and for the entropy losses and host-guest distortions required for confinement, as reported here from confinement free energies ensemble-averaged over all crystallographic locations in each aluminosilicate structure. The ratios of rate constants for these parallel isobutene dimerization and Prins condensation reactions depend only weakly on the nature of the aluminosilicate framework, because of the similar size and shape of their respective transition states and bound precursors. Transition states for secondary skeletal isomerization and cyclization of 2,5-DMH condensation products, however, are stabilized more effectively (relative to condensation transition states) within voids of intermediate size (BEA, MFI), leading to higher selectivity to secondary products. MFI cage-like structures specifically catalyze the conversion of 2,5-DMH to cyclic 1,4-dimethyl-cyclohexene isomers, direct precursors to *p*-xylene, with unique specificity.

© 2017 Published by Elsevier Inc.

1. Introduction

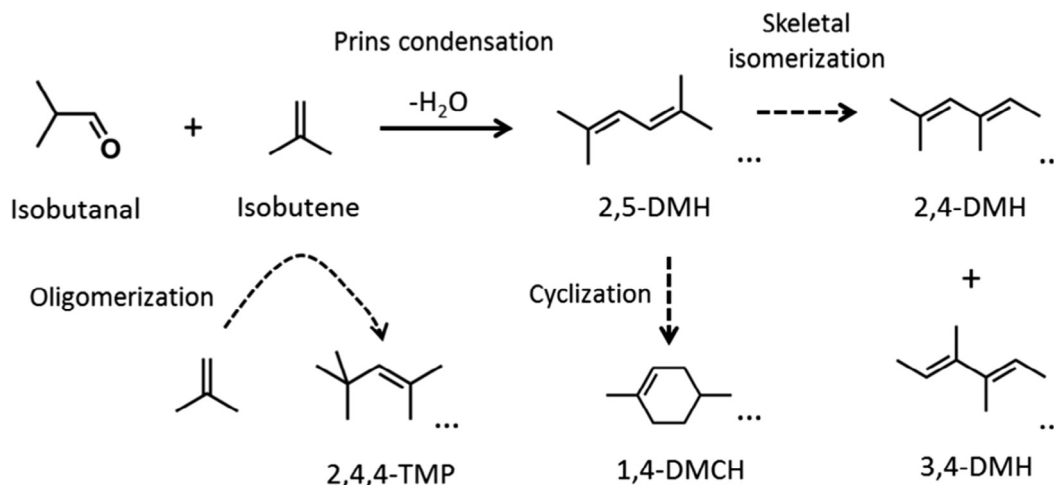
Isobutanol-isobutene Prins condensation reactions on solid Brønsted acids form 2,5-dimethyl-hexadiene regioisomers (2,5-DMH) [1–5] with backbones that can subsequently form *p*-xylene via dehydrocyclization reactions [6,7]. These condensation reactions involve co-reactants that can be derived from isobutanol [8–10] via dehydrogenation [11] and dehydration [12]. Secondary skeletal isomerization of 2,5-DMH regioisomers forms 2,4-DMH

and 3,4-DMH and cyclization of these regioisomers forms the double-bond isomers of 1,4-dimethyl-cyclohexene (1,4-DMCH) (Scheme 1) [5,13]. These reactions occur in parallel with isobutene oligomerization to form 2,4,4-trimethyl-pentene regioisomers (2,4,4-TMP) [5,14–16]. Non-coordinating basic titrants (2,6-di-*tert*-butyl-pyridine) fully suppress all aforementioned reactions on various solid acids (e.g. Keggin heteropolyacids, niobic acid, and mesoporous and microporous aluminosilicates) [5], reflecting that these reactions occur exclusively on Brønsted acid sites.

Acid strength and confinement effects combine to account for the diversity of solid acid catalysts in catalytic transformations [16–25]. The effects of acid strength were previously examined

* Corresponding author.

E-mail address: iglesia@berkeley.edu (E. Iglesia).



Scheme 1. Brønsted-acid-catalyzed reactions of isobutanol-isobutene mixtures.

through experiment and theory for Prins condensation and oligomerization reactions of isobutanol-isobutene mixtures [5]. Both reactions are mediated by kinetically-relevant C–C bond formation steps involving cationic transition states (TS), thus leading to higher reactivity for both reactions on stronger acids, because they form more stable conjugate anions at the TS [5,13,16]. Theoretical treatments of the elementary steps and intermediates involved indicate that the oligomerization TS (TS_{oligo}) is a full ion-pair on solids with a broad range of acid strength; the Prins condensation TS structures (TS_{prins}), in contrast, become full carbenium ions only on stronger acids, such as Keggin heteropolytungstates [5]. The lower charges at the TS_{prins} conjugate anion lead to smaller energy penalties than for TS_{oligo} as acid sites weaken, thus making weaker acids, such as niobic acid and aluminosilicates, more selective for Prins condensation than stronger acids, such as heteropolytungstate clusters.

The consequences of confinement within voids of molecular size remain unexplored and unexploited for Prins condensations. Aluminosilicates contain isolated protons that act as Brønsted acids; their acid strength is similar on aluminosilicates with different frameworks and Al content, as long as Al-atoms are isolated from one another in the structure [22,26]. These protons reside within voids that differ in size and shape among diverse crystalline frameworks, thus allowing TS structures of different size and shape to be stabilized to different extents depending on their fit within the confining voids [16,19,27,28]. As a result, mesoporous and microporous aluminosilicates can be used to probe the effects of confinement, in the absence of concomitant effects of acid strength, on Prins condensation and oligomerization catalysis.

Here, we report how the void structure of aluminosilicates (FAU, BEA, MFI, TON, and Al-MCM-41) influences the reactivity of confined protons in isobutanol-isobutene Prins condensation and isobutene oligomerization. On all samples, both reactions are limited by their respective C–C bond formation elementary step, but smaller voids preferentially stabilize bound isobutanol species. The ratio of Prins condensation to oligomerization rate constants ($k_{\text{prins}}/k_{\text{oligo}}$) remains essentially unaffected by the aluminosilicate void structure, because TS_{prins} and TS_{oligo} structures are similar in size and shape and consequently interact to the same extent with confining voids of different dimensions. Measured Prins condensation rate constants ($k_{\text{prins}}/K_{\text{al}}$, where K_{al} is the isobutanol adsorption equilibrium constant at a proton site) are larger on FAU than in aluminosilicate acids with larger (Al-MCM-41) or smaller (BEA, MFI, and TON) voids, as is also the case for measured oligomerization rate constants ($k_{\text{oligo}}/K_{\text{al}}$), because of the preferential stabilization of TS_{prins} relative to the smaller bound isobutanol species.

Ensemble averaging of the energies derived from density functional theory (DFT) for all configurations of bound intermediates throughout all accessible Al locations in aluminosilicate frameworks indicates that H-bonded isobutanol is the prevalent bound intermediate at all conditions of practical catalysis. DFT-derived free energies that account for van der Waals interactions, framework distortions required for effective host-guest contacts, and entropy losses brought forth by confinement represent the most accurate descriptors of Prins condensation turnover rates. These DFT-derived descriptors rigorously account for the consequences of size and shape (for transition states, bound precursors, and voids) on Prins condensation reactivity on acids with diverse void structures, in contrast with the spherical constructs typically used to describe voids and the effects of size on reactivity.

Secondary skeletal isomerization and cyclization of 2,5-DMH Prins condensation products are more prevalent in voids of intermediate size (MFI, BEA) than in smaller (TON) or larger (FAU, Al-MCM-41) voids. Specifically, MFI voids led to a high selectivity to 1,4-DMCH cyclization products. These trends appear to reflect that transition states that mediate the isomerization and cyclization of 2,5-DMH fit the voids of intermediate size better than TS_{prins} and thus gain more effective van der Waals stabilization conferred by interactions with the confining voids.

This study demonstrates the role of confinement within voids of molecular size in reactivity and selectivity for Prins condensation and oligomerization through a combination of kinetic assessment of elementary steps, rigorous turnover rate data on protons within diverse void structures, and theoretical treatments that account for dispersion forces, framework distortions, and entropy effects, which are the relevant effects and properties that combine to describe the effects of van der Waals contacts between voids and bound organic moieties. In doing so, the work described here represents a step toward the replacement of geometric descriptors of confinement with the free energies of bound intermediates and transition states in host-guest systems of significant catalytic interest.

2. Methods

2.1. Catalyst synthesis and characterization

H-BEA (Si/Al = 43.3) and H-MFI (Si/Al = 16.6, 29.2, and 43.8) were obtained from Zeolyst and H-Al-MCM-41 (Si/Al = 39.5) was obtained from Sigma-Aldrich. H-TON (Si/Al = 39) was prepared using known protocols [29]. H-USY (Union Carbide, Si/Al = 2.9)

was treated with aqueous $(\text{NH}_4)_2\text{SiF}_6$ (99%, Alfa Aesar) solutions at 348 K and then washed with deionized water to chemically remove extra framework Al species [23]. The Si and Al contents in each sample were measured by inductively-coupled plasma optical emission spectroscopy (ICP-OES; Galbraith Laboratories). For microporous aluminosilicates, the number of H^+ was determined from the amount of NH_3 evolved upon thermal treatment of their NH_4^+ -exchanged forms [23]. For H-Al-MCM-41, the number of H^+ was measured via titration with non-coordinating 2,6-di-*tert*-butylpyridine during isobutanol-isobutene condensation reactions at 473 K [5]. The sources, Al/Si ratios, H^+ densities and void size descriptors (the largest-cavity (LCD) and pore-limiting diameters (PLD) [30]) for all samples are shown in Table 1. These samples were treated in flowing dry air (Praxair, 99.999%, $1.67 \text{ cm}^3 \text{ g}^{-1} \text{ s}^{-1}$) at 823 K (at 0.025 K s^{-1}) for 5 h and then pressed, crushed, and sieved to retain 100–180 μm aggregates before catalytic measurements.

2.2. Catalytic rate measurements

Rates and selectivities were measured using protocols previously described in detail [5]. Isobutanol-isobutene reactants were contacted with the solid acids in a tubular quartz reactor (1.0 cm I.D.) with plug-flow hydrodynamics. The catalysts (20–400 mg) were treated in flowing air (Praxair, 99.999%, $1.67 \text{ cm}^3 \text{ g}^{-1} \text{ s}^{-1}$) at reaction temperature (0.0833 K s^{-1} ; 4 h hold). Isobutanol (Sigma-Aldrich, $\geq 99\%$) was introduced using a syringe pump (Cole Parmer, 74900 series); isobutene (Praxair, 99%) and He (Praxair, 99.999%) flows were metered using electronic mass flow controllers (Porter, Model 201). All transfer lines were kept at 433 K to prevent condensation. Molecular speciation and concentrations were determined by online gas chromatography (Agilent 6890) using a methyl silicone capillary column (Agilent HP-1, 50 m, 0.32 mm I.D., 1.05 μm film) and flame ionization detection. Speciation was confirmed from known standards and mass spectrometry of the molecules present in the reactor effluent. Turnover rates are reported from rates of formation normalized by the number of protons (Table 1). Product selectivities are reported on a carbon atom basis.

2.3. Computational methods

The stability of surface species and intermediates involved in the elementary steps that mediate isobutanol-isobutene Prins condensation and isobutene oligomerization on microporous and mesoporous aluminosilicates (H-FAU, H-BEA, H-MFI, H-TON, and H-Al-MCM-41) was assessed using periodic plane-wave density functional theory (DFT) as implemented in the Vienna ab initio simulation package (VASP) [31–34]. The Perdew-Burke-Ernzerhof (PBE) functional [35,36] was used to describe the exchange-correlation interactions of electrons; the projector

augmented-wave (PAW) pseudopotentials [37,38] with a cutoff energy of 396 eV were used to represent wavefunctions. Geometric optimizations were performed with a $(1 \times 1 \times 1)$ Γ -centered k-point mesh and convergence criteria of 1×10^{-6} eV for energies and 0.02 eV \AA^{-1} for forces on each atom. Grimme's D3BJ dispersion corrections [39,40] were included in each energy minimization step in order to accurately account for van der Waals interactions. DFT-derived harmonic vibrational frequencies were used to calculate thermal corrections to enthalpies, entropies, and Gibbs free energies for optimized structures [41]; the contributions of low-frequency modes ($< 60 \text{ cm}^{-1}$) in such structures were replaced by those for similar rotations in gaseous molecules to avoid significant underestimation of entropies [42].

The FAU structure ($a = b = c = 2.4345 \text{ nm}$; $\alpha = \beta = \gamma = 90^\circ$), obtained from the International Zeolite Association (IZA) website [43] henceforth) contains supercages (LCD 1.19 nm, Table 1) that are constructed by corner-sharing TO_4 ($\text{T} = \text{Si}^{4+}, \text{Al}^{3+}$) tetrahedra and connected via 12-membered-ring (MR) windows (PLD 0.67 nm, Table 1). The BEA structure ($a = b = 1.2632 \text{ nm}$, $c = 2.6186 \text{ nm}$; $\alpha = \beta = \gamma = 90^\circ$) contains straight 12-MR channels along the a and b axes, which are connected by tortuous channels along the c axis (LCD 0.69 nm, PLD 0.67 nm, Table 1). The MFI structure ($a = 2.0090 \text{ nm}$, $b = 1.9738 \text{ nm}$, $c = 1.3142 \text{ nm}$; $\alpha = \beta = \gamma = 90^\circ$) contains sinusoidal and straight 10-MR channels along the a and b axes (PLD 0.50 nm, Table 1), respectively, and intersections of these channels form larger ellipsoidal voids (LCD 0.70 nm, Table 1). The TON structure ($a = 1.4105 \text{ nm}$, $b = 1.7842 \text{ nm}$, $c = 0.5256 \text{ nm}$; $\alpha = \beta = \gamma = 90^\circ$) contains only one-dimensional straight channels (LCD 0.57 nm, PLD 0.57 nm, Table 1). FAU, BEA, MFI, and TON structures have 1, 9, 12, and 4 distinct T-sites, with 4, 6, 17, and 26 distinct O-sites. The isomorphous substitution of Si^{4+} with Al^{3+} at a T-site creates a charge imbalance compensated by a proton. These proton locations are denoted as Alx-Oy(H) , where x and y are the T-site and O-site using the numbering system dictated by convention [43]. A supercell consisting of 4 unit cells along the c axis for TON and single unit cells for FAU, BAE, and MFI were used as models; these cells contain similar numbers of atoms and proton densities smaller than $0.24 \text{ H}^+ \text{ nm}^{-3}$ in order to prevent interactions among bound species in adjacent periodic images. Amorphous aluminosilicate slabs ($\text{Si}_{59}\text{AlO}_{124}\text{H}_9$ per unit cell) were used to model H-Al-MCM-41 surfaces, using structures and protocols previously described [5]; the proton sites on these slabs show deprotonation energies (DPE) similar to those in microporous aluminosilicates (1212 vs. $1201 \pm 11 \text{ kJ mol}^{-1}$ [5,26]), thus providing models to assess acid-catalyzed elementary steps on zeolitic proton sites without any effects of confinement.

Adsorption free energies (ΔG_{ads} , e.g. isobutanol and isobutene) are given by the free energy for the bound species (G_{guest^*}) relative to their gaseous form (G_{guest}) and a proton site (G_{ZH}):

$$\Delta G_{\text{ads}} = G_{\text{guest}^*} - G_{\text{guest}} - G_{\text{ZH}} \quad (1)$$

Table 1
Physicochemical properties of microporous and mesoporous aluminosilicates used in this study.

Sample	Source	Si/Al ratio ^a	H^+/Al	LCD ^d (nm)	PLD ^e (nm)
H-Al-MCM-41	Sigma-Aldrich	39.5	0.35 ^b	2.5	2.5
H-FAU	[23]	7.5	0.37 ^c	1.19	0.67
H-BEA	Zeolyst	43.3	1.0 ^c	0.69	0.67
H-MFI-1	Zeolyst	16.6	0.65 ^c	0.70	0.50
H-MFI-2	Zeolyst	29.2	0.78 ^c	0.70	0.50
H-MFI-3	Zeolyst	43.8	1.0 ^c	0.70	0.50
H-TON	[29]	39	0.55 ^c	0.57	0.57

^a Elemental analysis (ICP-OES; Galbraith Laboratories).

^b Titration by 2,6-di-*tert*-butylpyridine during catalysis [5].

^c NH_3 evolution from NH_4^+ -exchanged samples [23].

^d Largest-cavity diameter [30].

^e Pore-limiting diameter [30].

Fast proton migration throughout all four O-atoms at each Al T-site (evident from infrared spectra of bound pyridine on FAU [18] and from DFT treatments [26]) equilibrates protons among all locations. The proton free energy ensemble-averaged over all positions ($\langle G_{ZH} \rangle$) is given by

$$\langle G_{ZH} \rangle = \frac{\sum_{i=1}^4 \left[G_{ZH,i} \exp\left(\frac{-G_{ZH,i}}{k_B T}\right) \right]}{\sum_{i=1}^4 \exp\left(\frac{-G_{ZH,i}}{k_B T}\right)} \quad (2)$$

where $G_{ZH,i}$ is the free energy at the proton location i for each Al T-site and k_B is the Boltzmann constant. Similar ensemble-averaging procedures give the free energy for a species bound at a given Al T-site ($\langle G_{\text{guest}^*} \rangle$):

$$\langle G_{\text{guest}^*} \rangle = \frac{\sum_{i=1}^4 \left[G_{\text{guest}^*,i} \exp\left(\frac{-G_{\text{guest}^*,i}}{k_B T}\right) \right]}{\sum_{i=1}^4 \exp\left(\frac{-G_{\text{guest}^*,i}}{k_B T}\right)} \quad (3)$$

where $G_{\text{guest}^*,i}$ is the free energy for species bound to location i at each Al T-site. The ensemble-averaged adsorption free energies over all four proton locations ($\langle \Delta G_{\text{ads}} \rangle$, Scheme 2) are thus given by

$$\langle \Delta G_{\text{ads}} \rangle = \langle G_{\text{guest}^*} \rangle - G_{\text{guest}} - \langle G_{ZH} \rangle \quad (4)$$

The exponential averaging of $\langle \Delta G_{\text{ads}} \rangle$ values over all accessible Al T-site locations in an aluminosilicate framework gives ensemble-averaged adsorption free energies for guest molecules ($\overline{\langle \Delta G_{\text{ads}} \rangle}$) [28]:

$$\overline{\langle \Delta G_{\text{ads}} \rangle} = -k_B T \ln \left(\sum_j^{N_{\text{T-site}}} \exp\left(-\frac{\langle \Delta G_{\text{ads}} \rangle_j}{k_B T}\right) P_{\text{T-site},j} \right) \quad (5)$$

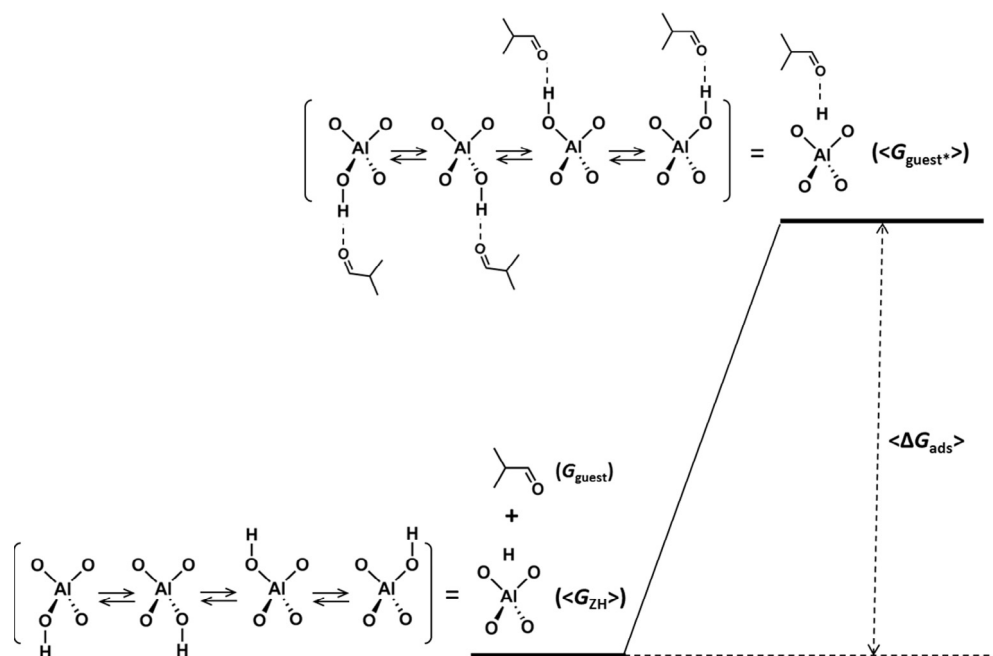
Here, $N_{\text{T-site}}$ is the number of distinct Al T-site locations for the framework and $P_{\text{T-site},j}$ is the probability of the Al-atom residing at T-site j . The Al distributions of aluminosilicates that determine $P_{\text{T-site},j}$ are sensitive to the synthetic protocols, except for frameworks with one T-site location (e.g. FAU) or those for which all T-sites reside within similar void environments (e.g. BEA and TON

[28]); such Al distributions are rarely available from experiments [44,45]. Here, Al-atoms are assumed to be uniformly distributed among all T-sites for TON and BEA. MFI frameworks exhibit very distinct void environments at channel and intersection environments [22,28]; as a result, we examine here two plausible distributions of Al-atoms: (i) uniformly distributed among all T-sites and (ii) uniformly distributed only among T-sites at intersections (T1 and T5–T12 sites). Only one T-site is considered for Al placement in Al-MCM-41, because of its amorphous nature and the large and weakly-interacting nature of its channels [5]. The values of $P_{\text{T-site},j}$ are thus given by [28]

$$P_{\text{T-site},j} = \frac{N_j}{\left(\sum_j^{N_{\text{T-site}}} N_j\right)} \quad (6)$$

where N_j is the number of locations of T-site j per unit cell of the framework.

The size and shape of 2,5-DMH Prins condensation products and their skeletal (2,4-DMH, 3,4-DMH) and cyclic (1,4-DMCH) isomers were estimated from their isoelectronic density surfaces at $0.0015 e a_0^{-3}$ (e is the charge of a single proton; a_0 is the Bohr radius) [46]. Geometry optimizations were performed using the Berny geometry algorithm [47] and dispersion-corrected spin-component-scaled double-hybrid DSD-PBEP86-D3BJ functionals [48], which approach ab initio level accuracies at accessible computational costs. The triple- ζ , polarized valence def2-TZVP basis set [49] implemented in the Gaussian software package [50] was used for the geometry optimizations. Energies and the maximum residual forces on each atom were converged to 1.0×10^{-8} Ha and 1.5×10^{-5} Ha Bohr $^{-1}$, respectively, to obtain optimized structures. The length of a molecule is defined as the diameter of the smallest sphere that can fully contain it, whereas its width is defined as the diameter of the smallest circle that can contain its projected area onto a plane perpendicular to the longest dimension of the molecule.



Scheme 2. Schematic of ensemble-averaged adsorption free energies ($\langle \Delta G_{\text{ads}} \rangle$) over all accessible proton locations (Al T-sites) for adsorption of guest molecules on aluminosilicates (isobutanol used as an illustrative example). $\langle G_{ZH} \rangle$ (Eq. (2)) and $\langle G_{\text{guest}^*} \rangle$ (Eq. (3)) are ensemble-averaged free energies for protons and bound configurations of guest molecules, respectively; G_{guest} is the free energy for the guest molecule in the gas phase.

3. Results and discussion

3.1. Effects of isobutanal and isobutene pressures on Prins condensation and oligomerization turnover rates

Isobutanal-isobutene mixtures form 2,5-dimethyl-hexadiene regioisomers (2,5-DMH) via Prins condensation and also convert isobutene co-reactants to 2,4,4-trimethyl-pentene regioisomers (2,4,4-TMP) via oligomerization on all aluminosilicates (H-TON, H-MFI, H-BEA, H-FAU, and H-Al-MCM-41) (Scheme 1), as also observed on Keggin heteropolytungstic acid clusters and niobic acid powders [5]. Skeletal isomerization and cyclization of the primary products formed in these reactions also occur to form 2,4-DMH and 3,4-DMH via skeletal isomerization and 1,4-dimethyl-cyclohexene (1,4-DMCH) via cyclization of 2,5-DMH (Scheme 1) [5]. These secondary interconversions become more prevalent as conversion increases (Section 3.5). Regioisomers with a given backbone interconvert rapidly on all acids at the conditions of this study (473 K; 0–4 kPa isobutanal/isobutene) to form equilibrated mixtures [5,15,16], thus allowing each skeletal structure to be treated as a lumped product in all kinetic analyses that follow.

Isobutanal-isobutene Prins condensation rates (r_{prins} ; combined rates of formation of 2,5-DMH and its skeletal and cyclic isomers) on H-FAU increased monotonically with isobutene and isobutanal pressures and then reached constant values at higher pressures (Figs. 1a and 2). The rates of isobutene oligomerization (r_{oligo} ; formation rates of 2,4,4-TMP regioisomers) on H-FAU showed a stronger dependence on isobutene pressure than Prins condensation rates (Fig. 1b), while oligomerization rates decreased with increasing isobutanal pressure (Fig. 2). As shown previously on H-Al-MCM-41 [5] and discussed below, such kinetic effects of pressure on r_{prins} and r_{oligo} are evidence for C–C bond formation as the sole kinetically-relevant step for both reactions. These steps involve the reactions of a gaseous isobutene with either an isobutanal (Prins condensation) or an isobutene (oligomerization) bound at the location initially containing the proton. The common involvement of a gaseous isobutene in both kinetically-relevant steps leads to $r_{\text{prins}}/r_{\text{oligo}}$ ratios that depend linearly on the isobutanal/isobutene ratios at all pressures, as shown on microporous H-FAU, H-BEA, H-MFI, and H-TON (Fig. 3) and on mesoporous H-Al-MCM-41 [5]; these ratios are determined by the relative coverages of bound

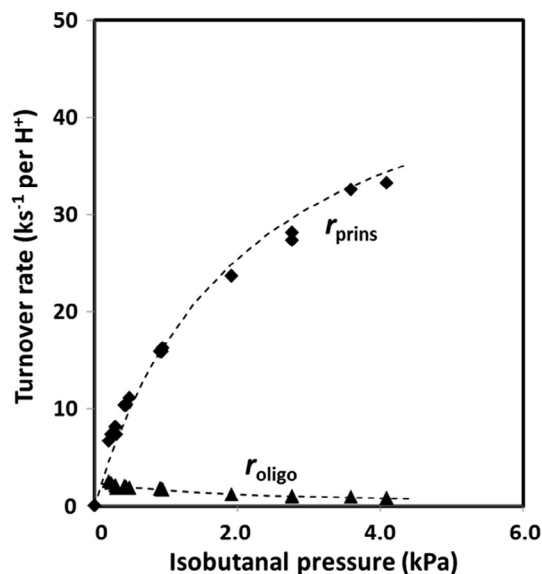


Fig. 2. Effects of isobutanal pressure on isobutanal-isobutene Prins condensation and isobutene oligomerization turnover rates (r_{prins} , r_{oligo}) (H-FAU; 473 K; 0–4.2 kPa isobutanal; 1.0 kPa isobutene). Dashed curves represent regressed fits of r_{prins} and r_{oligo} to the functional forms of Eqs. (7) and (8), respectively.

isobutanal and isobutene and by their respective reactivities with isobutene in C–C bond formation elementary steps.

These effects of isobutanal and isobutene pressures on r_{prins} and r_{oligo} (Figs. 1–2) and of their pressure ratios on selectivity ($r_{\text{prins}}/r_{\text{oligo}}$; Fig. 3) resemble those observed on mesoporous acids that differ significantly from these aluminosilicates in their acid strength [5]. Rates on aluminosilicates are accurately described by

$$r_{\text{prins}} = \frac{k_{\text{prins}} P_{\text{al}} P_{\text{ene}}}{1 + K_{\text{al}} P_{\text{al}} + K_{\text{ene}} P_{\text{ene}} + K_{\text{al-ene}} P_{\text{al}} P_{\text{ene}} + K_{\text{al-al}} P_{\text{al}}^2 + K_{\text{ene-ene}} P_{\text{ene}}^2} \quad (7)$$

$$r_{\text{oligo}} = \frac{k_{\text{oligo}} P_{\text{ene}}^2}{1 + K_{\text{al}} P_{\text{al}} + K_{\text{ene}} P_{\text{ene}} + K_{\text{al-ene}} P_{\text{al}} P_{\text{ene}} + K_{\text{al-al}} P_{\text{al}}^2 + K_{\text{ene-ene}} P_{\text{ene}}^2} \quad (8)$$

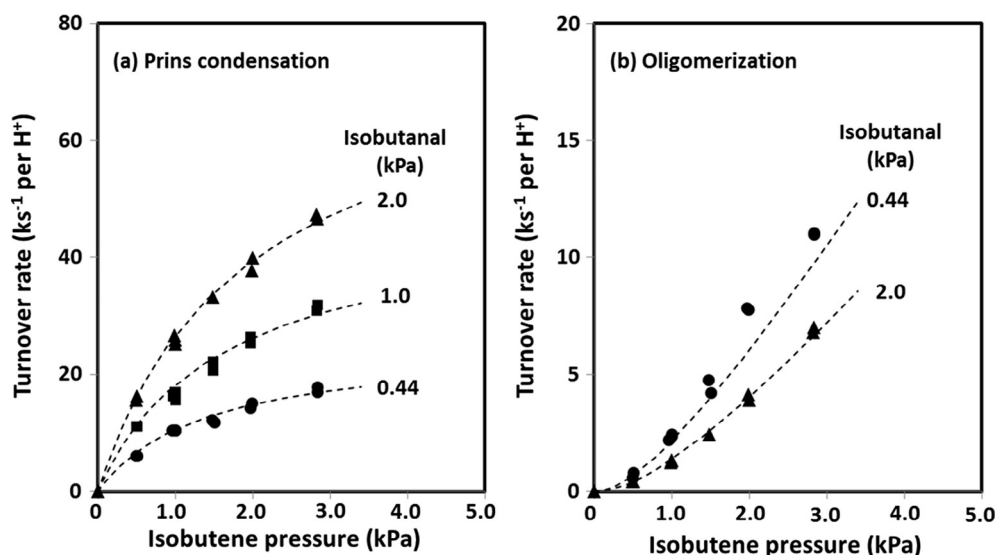


Fig. 1. Effects of isobutene pressure on (a) isobutanal-isobutene Prins condensation turnover rates and (b) isobutene oligomerization turnover rates (H-FAU; 473 K; 0–2.0 kPa isobutanal; 0–3.0 kPa isobutene). Dashed curves in (a) and (b) represent regressed fits to the functional forms of Eqs. (7) and (8), respectively.

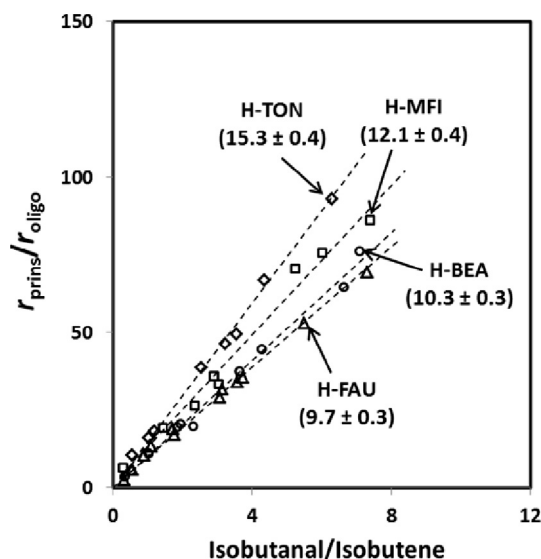


Fig. 3. Effects of isobutanal/isobutene reactant ratio on ratios of isobutanal-isobutene Prins condensation and isobutene oligomerization turnover rates (H-FAU (Δ); H-BEA (\circ); H-MFI-3 (\square); H-TON (\diamond); 473 K; 0–4 kPa isobutanal; 0–3 kPa isobutene). Dashed lines represent linear regression fits and respective regressed slopes are shown beside the lines.

These two rate equations are also consistent with the observed dependence of $r_{\text{prins}}/r_{\text{oligo}}$ ratios on the ratio of reactant pressures. In Equations (7) and (8), P_{al} and P_{ene} are the isobutanal and isobutene pressures; k_{prins} and k_{oligo} represent the second-order rate constants for Prins condensation and oligomerization in their respective kinetically-relevant elementary steps; K_{al} , K_{ene} , $K_{\text{al-ene}}$, $K_{\text{al-al}}$, and $K_{\text{ene-ene}}$ are the adsorption equilibrium constants for lumped bound species consisting of all possible configurations of bound isobutanal and isobutene monomers (e.g. H-bonded isobutanal and 1-hydroxy-*iso*-butoxide derived from isobutanal; π -bonded isobutene, *iso*-butoxide, and *tert*-butoxide derived from isobutene [5]) and of isobutanal-isobutene, isobutanal-isobutanal, and isobutene-isobutene dimers at proton sites.

Equations (7) and (8) are consistent with the sequence of elementary steps proposed previously based on experimental and theoretical analyses on mesoporous acids [5]. Isobutanal adsorbs through H-bonding with a proton (Step 1, Scheme 3) and forms a C–C bond via nucleophilic attack at the carbonyl C-atom of the H-bonded isobutanal by the terminal C-atom in the C=C bond of a gaseous isobutene to form a γ -hydroxy- C_8 alkoxide (Steps 2–3, Scheme 3). Subsequent deprotonation and H_2O elimination steps (Steps 4–5, Scheme 3) form the C_8 diene isomer products (2,5-DMH). In contrast, *tert*-butoxides are formed via the adsorption of isobutene on protons as π -bonded precursors that convert to *tert*-butoxides intermediates as they form C–C bonds with isobutene (Step 1', Scheme 3). Nucleophilic attack at the tertiary C-atom of the *tert*-butoxide by the terminal C-atom in the C=C bond of a gaseous isobutene forms C_8 alkoxides (Steps 2'–3', Scheme 3), which then convert to π -bonded C_8 alkene dimers (2,4,4-TMP) that desorb to form the respective gaseous alkenes (Step 4', Scheme 3).

The measured effects of reactant pressures on rates (Figs. 1 and 2), taken together with DFT-derived free energies along the Prins condensation and oligomerization reaction coordinates [5], indicate that C–C bond formation is the sole kinetically-relevant elementary step for both Prins condensation and oligomerization reactions on aluminosilicates, as also found on other solid acids [5]. Equations (7) and (8) lead to $r_{\text{prins}}/r_{\text{oligo}}$ ratios that are interpreted mechanistically as follows:

$$\frac{r_{\text{prins}}}{r_{\text{oligo}}} = \frac{k_{\text{prins}}P_{\text{al}}}{k_{\text{oligo}}P_{\text{ene}}} \quad (9)$$

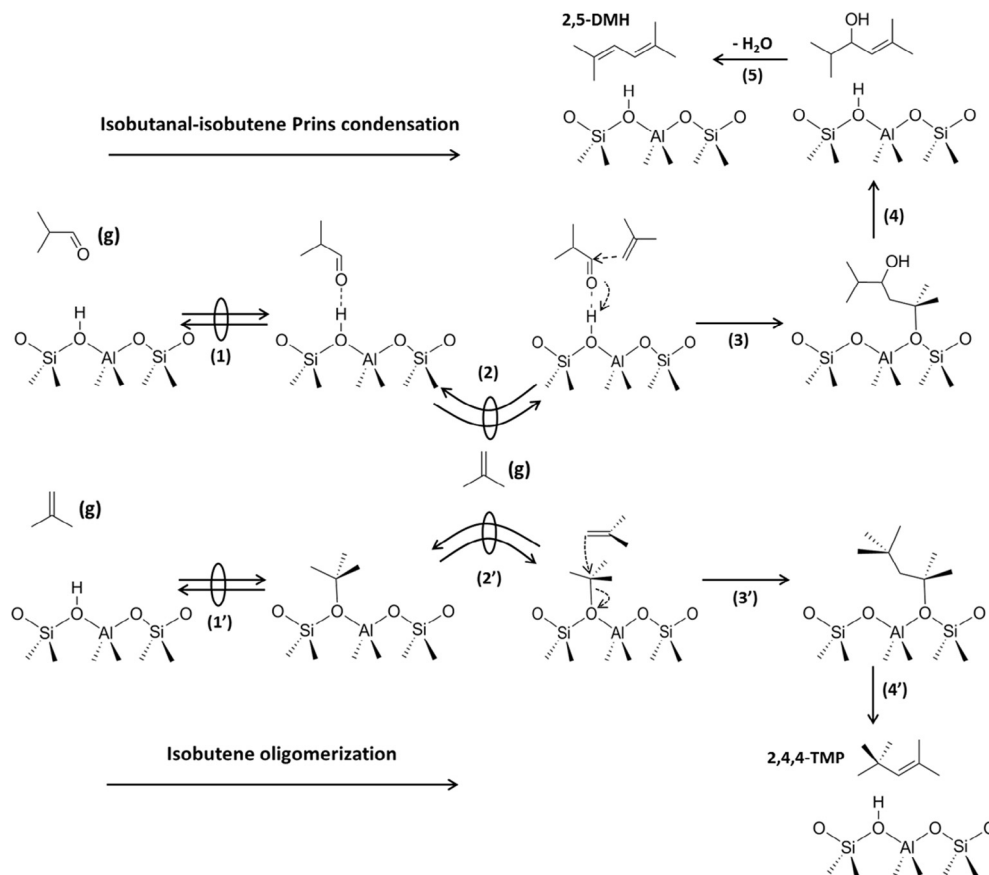
These ratios are in agreement with data (Fig. 3) and serve to define the chemical meaning of the slopes in Fig. 3 as the $k_{\text{prins}}/k_{\text{oligo}}$ ratio in Equation (9); this ratio denotes the intrinsic reactivity in Prins condensation and oligomerization reactions for each solid acid as defined by the rate constants of their respective kinetically-relevant steps.

The k_{prins} and k_{oligo} parameters obtained by regressing the rate data in Figs. 1 and 2 on H-FAU to the functional forms of Equations (7) and (8), respectively, are 49 ± 7 and $5.1 \pm 0.8 \text{ ks}^{-1} \text{ kPa}^{-2} \text{ per H}^+$ (473 K; Table 2). These k_{prins} and k_{oligo} values are larger than on mesoporous aluminosilicates of similar acid strength (H-Al-MCM-41 [5]; $k_{\text{prins}} 12 \pm 2 \text{ ks}^{-1} \text{ kPa}^{-2} \text{ per H}^+$, $k_{\text{oligo}} 1.2 \pm 0.3 \text{ ks}^{-1} \text{ kPa}^{-2} \text{ per H}^+$; Table 2). Such reactivity enhancements reflect the stabilization of the kinetically-relevant C–C coupling TS structures (with respect to their respective gaseous reactants) through van der Waals contacts within the molecular-size voids present in crystalline aluminosilicates, as discussed in detail in Section 3.4 in the context of DFT treatments used to confirm these mechanistic hypotheses. These confinement effects are also evident in the regressed values of the adsorption equilibrium constants, which are larger on H-FAU than on mesoporous H-Al-MCM-41 (e.g. $K_{\text{al}} 0.9 \pm 0.2$ vs. $0.3 \pm 0.1 \text{ kPa}^{-1}$; $K_{\text{ene}} 0.7 \pm 0.2$ vs. $0.3 \pm 0.1 \text{ kPa}^{-1}$; 473 K; Table 2).

In contrast with these differences in rate and equilibrium constants, the $k_{\text{prins}}/k_{\text{oligo}}$ ratios are similar on H-FAU and H-Al-MCM-41 (9.7 ± 0.3 vs 10.3 ± 0.2 , Table 2), in spite of their very different reactivities. These similar ratios reflect C–C coupling TS structures for Prins condensation and oligomerization that are of similar size (DFT-derived van der Waals volume: 0.153 vs. 0.144 nm^3 [5]); they also confirm the similar acid strength of microporous and mesoporous aluminosilicates, in light of the strong sensitivity of $k_{\text{prins}}/k_{\text{oligo}}$ ratios to acid strength established for mesoporous acids that differ in acid strength [5]. Such sensitivity to acid strength reflects TS_{prins} structures that become a full ion-pair only on the strongest acids, thus acting as a sensitive experimental descriptor of acid strength.

Similar $k_{\text{prins}}/k_{\text{oligo}}$ values were also measured on H-BEA (10.3 ± 0.3), H-MFI (12.1 ± 0.4), and H-TON (15.3 ± 0.3) (Fig. 3) in spite of voids that differ significantly in size and geometric details (0.57–1.19 nm largest-cavity diameter [30]; Table 1). We conclude from the insensitivity of $k_{\text{prins}}/k_{\text{oligo}}$ ratios to the geometry of the confining voids that C–C coupling TS structures for Prins condensation and oligomerization reactions can establish similar van der Waals contacts with void walls. These findings allow the mechanistic discourse that follows to address the effects of confinement only on Prins condensation turnovers, while the conclusions remain applicable to isobutene oligomerization events.

The effects of isobutene pressure on Prins condensation rates (Figs. 1a and 4a) and of isobutanal pressure on Prins condensation rates (Figs. 2 and 4b) are similar on BEA and FAU, indicative of similar mechanistic underpinnings that can be accurately captured by the functional form of Equation (7). The k_{prins} , K_{al} , and K_{ene} values on BEA are larger than on FAU (60 ± 15 vs. $49 \pm 7 \text{ ks}^{-1} \text{ kPa}^{-2} \text{ per H}^+$, 4 ± 1 vs. $0.9 \pm 0.2 \text{ kPa}^{-1}$, 0.8 ± 0.4 vs. $0.7 \pm 0.2 \text{ kPa}^{-1}$, Table 2), consistent with smaller voids in BEA (0.69 nm [30], Table 1) than in FAU (1.19 nm [30], Table 1), which provide more effective van der Waals contacts for both TS structures and bound intermediates present within such voids. The ratio of the respective K_{al} values on BEA and FAU (4.4 ± 0.2 , Table 2) is much larger than their K_{ene} ratios (1.1 ± 0.3 , Table 2), indicating that isobutanal becomes favored over isobutene as the predominant adsorbed species as the confining voids become smaller. These trends are consistent with DFT-derived adsorption free energies for adsorbed species



Scheme 3. Proposed elementary steps involved in isobutanol-isobutene Prins condensation and isobutene oligomerization reactions on aluminosilicates. Quasi-equilibrated steps are noted by an empty oval symbol placed over a set of double arrows.

Table 2

Rate constants and adsorption constants obtained from regression of the pressure effects on Prins condensation and oligomerization turnover rates (at 473 K) to the respective functional forms of Eqs. (7) and (8) for H-Al-MCM-41, H-FAU and H-BEA acids.

Catalyst	H-Al-MCM-41 ^a	H-FAU ^b	H-BEA ^c
k_{prins} ($\text{ks}^{-1} \text{kPa}^{-2}$ per H^+)	12 ± 2	49 ± 7	60 ± 15
k_{oligo} ($\text{ks}^{-1} \text{kPa}^{-2}$ per H^+)	1.2 ± 0.3	5.1 ± 0.8	5.8 ± 1.5
K_{al} (kPa^{-1})	0.3 ± 0.1	0.9 ± 0.2	4 ± 1
K_{ene} (kPa^{-1})	0.3 ± 0.1	0.7 ± 0.2	0.8 ± 0.4
$K_{\text{al-ene}}$ (kPa^{-2})	0.17 ± 0.02	0.20 ± 0.05	0.42 ± 0.06
$K_{\text{al-al}}$ (kPa^{-2})	– ^d	– ^d	– ^d
$K_{\text{ene-ene}}$ (kPa^{-2})	– ^d	– ^d	– ^d

^a Adapted from [5].

^b From data in Figs. 1 and 2.

^c From Prins condensation rate data in Fig. 4 and oligomerization rate data in Fig. S1 in Supporting Information (SI).

^d Not measurable from the regression fits, because the error is insensitive to the value of the parameter.

derived from isobutanol and isobutene and described in detail in Section 3.3.

Prins condensation rates increased linearly with isobutene pressure on MFI, as also observed on FAU and BEA, but these effects became weaker with increasing isobutene pressure (Fig. 5a). Prins condensation rates on MFI decreased slightly with increasing isobutanol pressure (25.3–21.8 ks^{-1} from 0.5 to 4.0 kPa isobutanol; Fig. 5b), in sharp contrast with the monotonic increase evident on FAU (Fig. 2) and BEA (Fig. 4b). These inhibition effects by one of the reactants indicate that isobutanol dimers reach kinetically-detectable coverages and coexist with bound isobutanol mono-

mers on MFI. MFI protons are predominantly located at cage-like intersections (0.70 nm diameter, Table 1) between 10-MR straight (0.53×0.56 nm) and sinusoidal (0.51×0.55 nm) channels, and 9 of the 12 T-sites in MFI reside at such intersections (Section 2.3) for Si/Al ratios above 10–15 [22]. We surmise from the negative rate dependence on isobutanol pressure (Fig. 5b) that these cage-like structures provide particularly effective van der Waals contacts with the adsorbed species (e.g. H-bonded isobutanol and isobutanol dimers) compared with BEA channels of similar diameter (0.69 nm, Table 1) but uniform cylindrical shape, possibly because bound species can also interact with the “dimpled” surfaces provided by the interconnecting channels in MFI. Such van der Waals interactions lead to larger K_{al} values on MFI than on BEA and to near-saturation coverages of isobutanol-derived monomers on MFI even at the low isobutanol pressures in this study (0.2–4.0 kPa, Fig. 5b), consistent with DFT-derived adsorption energies described in Section 3.3 for these bound species within MFI and BEA voids.

At near-saturation coverages of isobutanol-derived species, the low concentrations of bare protons lead to a small first denominator term in Equation (7):

$$r_{\text{prins}} = \frac{k_{\text{prins}} P_{\text{ene}}}{1 + \frac{K_{\text{ene}} P_{\text{ene}}}{K_{\text{al}} P_{\text{al}}} + \frac{K_{\text{al-ene}} P_{\text{ene}}^2}{K_{\text{al}} P_{\text{al}}} + \frac{K_{\text{al-al}} P_{\text{al}}}{K_{\text{al}}} + \frac{K_{\text{ene-ene}} P_{\text{ene}}^2}{K_{\text{al}}}} \quad (10)$$

As a result, rate constants and adsorption constants become measurable only as ratios with respect to K_{al} (e.g. $k_{\text{prins}}/K_{\text{al}}$, $K_{\text{ene}}/K_{\text{al}}$). Equation (10) accurately describes all rate data on MFI (Fig. 5) with the regressed parameters shown in Table 3, where these parameters are compared on the same basis to those measured on the other cat-

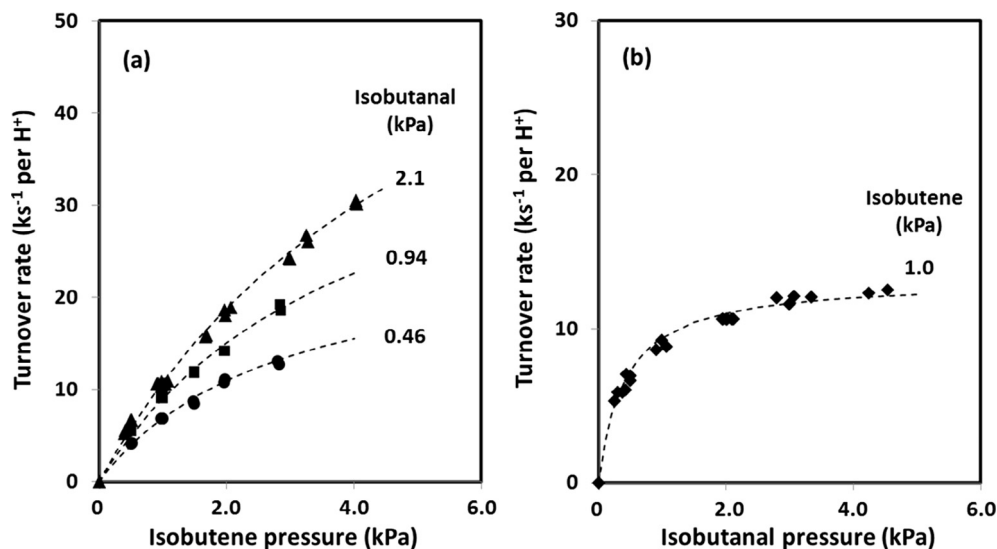


Fig. 4. Effects of (a) isobutene pressure and (b) isobutanal pressure on isobutanal-isobutene Prins condensation turnover rates (H-BEA; 473 K; 0–4.5 kPa isobutanal; 0–4.5 kPa isobutene). Dashed curves represent regressed fits to the functional form of Eq. (7).

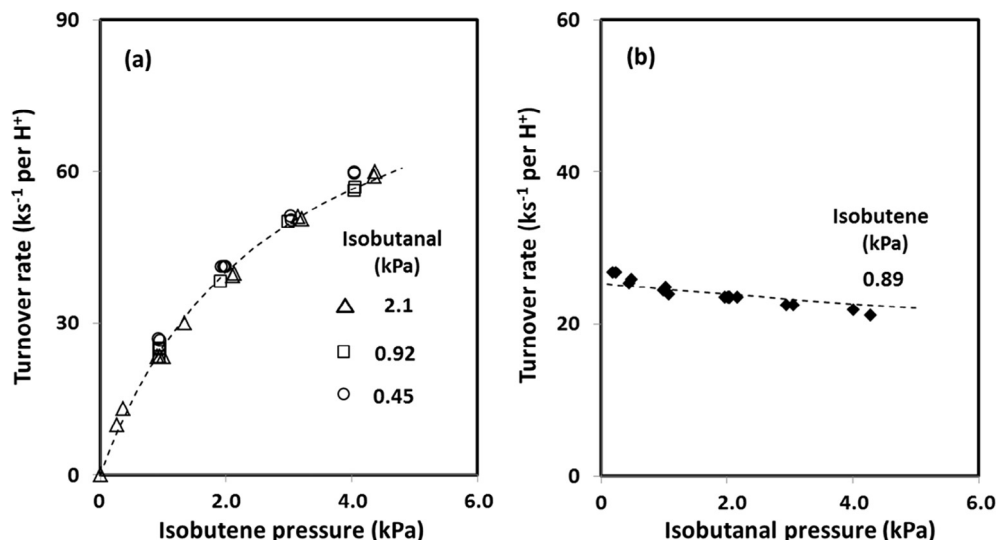


Fig. 5. Effects of (a) isobutene pressure and (b) isobutanal pressure on isobutanal-isobutene Prins condensation turnover rates (H-MFI-3 (Si/Al 43.8); 473 K; 0–4.5 kPa isobutanal; 0–4.5 kPa isobutene). Dashed curves represent regressed fits to the functional form of Eq. (10).

alysts (for which the individual kinetic and adsorption constants are independently accessible in the experiments as shown in Table 2).

The effects of isobutanal and isobutene pressures on condensation rates on TON (Fig. 6) and BEA (Fig. 4) are similar, even though TON protons reside within straight channels (0.57 nm, Table 1) smaller than those in H-BEA (0.69 nm, Table 1). The regressed k_{prins}

and K_{al} values on TON from rate data and Equation (7) are $380 \pm 370 \text{ ks}^{-1} \text{ kPa}^{-2} \text{ per H}^+$ and $26 \pm 25 \text{ kPa}^{-1}$, respectively (473 K, Table S1, SI); their very large uncertainties reflect the near-saturation coverages of isobutanal-derived species, which, as in the case of MFI, preclude accurate independent measurements of k_{prins} and K_{al} . As a consequence, only the ratios of rate

Table 3
Regressed Prins condensation rate constants and adsorption constants on microporous and mesoporous aluminosilicates.

Catalyst	H-Al-MCM ^a	H-FAU ^a	H-BEA ^a	H-MFI ^b	H-TON ^b
$k_{\text{prins}}/K_{\text{al}}$ (ks ⁻¹ kPa ⁻¹ per H ⁺)	40 ± 10	54 ± 6	15 ± 1	38 ± 1	11.8 ± 0.3
$K_{\text{ene}}/K_{\text{al}}$	1.0 ± 0.1	0.78 ± 0.06	0.20 ± 0.07	– ^c	0.21 ± 0.01
$K_{\text{al-ene}}/K_{\text{al}}$ (kPa ⁻¹)	0.6 ± 0.2	0.22 ± 0.01	0.11 ± 0.02	0.39 ± 0.02	0.08 ± 0.01
$K_{\text{al-al}}/K_{\text{al}}$ (kPa ⁻¹)	– ^c	– ^c	– ^c	0.04 ± 0.02	– ^c
$K_{\text{ene-ene}}/K_{\text{al}}$ (kPa ⁻¹)	– ^c	– ^c	– ^c	– ^c	– ^c

^a Adapted from Table 2.

^b From regressed fits of data (473 K) for H-MFI (Fig. 5) and H-TON (Fig. 6) using the functional form of Eq. (10).

^c Not measurable from the regression fits, because the error is insensitive to the value of the parameter.

constants and adsorption constants to K_{al} on TON can be measured accurately (Table 3). The regressed k_{prins}/K_{al} values on TON ($11.8 \pm 0.3 \text{ ks}^{-1} \text{ kPa}^{-1}$ per H^+ ; 473 K, Table 3) are smaller than on MFI ($38 \pm 1 \text{ ks}^{-1} \text{ kPa}^{-1}$) or BEA ($15 \pm 1 \text{ ks}^{-1} \text{ kPa}^{-1}$), reflecting TS_{prins} structures are less effectively stabilized (relative to the smaller isobutanal-derived bound species) in TON channels than in larger MFI and BEA voids, because of the lattice and TS distortions required for effective van der Waals contacts in TON, as shown by DFT treatments of the Prins condensation reaction coordinates on TON, MFI, and BEA frameworks in Section 3.4.

The successful descriptions of Prins condensation and oligomerization reactivity using Equations (7) and (8) support the mechanistic conclusions that protons catalyze C–C coupling via kinetically-relevant bimolecular transition states involving interactions of unbound isobutene with bound species derived from isobutanal or isobutene interacting with protons. The broad range of k_{prins}/K_{al} values among these aluminosilicates ($12\text{--}60 \text{ ks}^{-1} \text{ kPa}^{-1}$ per H^+ , Table 3) reflects the consequences of the confining voids for the relative stabilization of the TS_{prins} and the bound isobutanal-derived species, as a result of their different sizes and shapes.

Next, we examine how these k_{prins}/K_{al} ratios vary with geometric descriptors of the aluminosilicate hosts (Section 3.2). These trends are further examined using theoretical assessments of the van der Waals interactions and concomitant structural distortions and entropy losses brought forth by the van der Waals contacts responsible for these confinement effects (Sections 3.3–3.4).

3.2. Effects of confinement on the stability of C–C bond formation transition states

The k_{prins}/K_{al} parameters in Equation (10) are related to free energies ($\Delta G_{prins}^\ddagger$) through the formalism of transition state theory:

$$\frac{k_{prins}}{K_{al}} = \frac{k_B T}{h} \exp\left(-\frac{\Delta G_{prins}^\ddagger}{k_B T}\right) \quad (11)$$

This free energy reflects, in turn, the difference between the isobutanal–isobutene C–C coupling TS (G_{prins}^\ddagger) and the sum of a H-bonded isobutanal (G_{al} ; the predominant configuration, Section 3.3) and a gaseous isobutene (G_{ene}):

$$\Delta G_{prins}^\ddagger = G_{prins}^\ddagger - G_{al} - G_{ene} \quad (12)$$

as illustrated by the minimum energy reaction coordinate in Scheme 4. Thus, the magnitude of $\Delta G_{prins}^\ddagger$ depends on the different ability of the TS and the bound isobutanal to establish van der Waals contacts with the confining inorganic host. H-bonded isobutanal species are much smaller (0.435 nm, defined hereinforth as the diameter of a sphere of the same volume as the van der Waals volume of each species) than TS_{prins} (0.535 nm) [5]. Thus, k_{prins}/K_{al} values would sense confinement through the preferential stabilization of either the bound precursor or TS_{prins} as voids vary in size or shape.

Fig. 7 shows that k_{prins}/K_{al} values in FAU are slightly larger than in mesoporous Al-MCM-41 (54 ± 6 vs. $40 \pm 10 \text{ ks}^{-1} \text{ kPa}^{-1}$ per H^+ , 473 K), indicative of a weak but preferential stabilization of TS_{prins} over H-bonded isobutanals within the smaller voids in FAU, but not within the larger mesopores in Al-MCM-41; this trend is also evident from theoretical treatments that show how such larger pores do not allow significant van der Waals contacts between organic moieties and the inorganic hosts (Section 3.4). These k_{prins}/K_{al} values, however, decrease as voids become smaller than the FAU cages, as in BEA and TON structures (Fig. 7), suggesting that TS_{prins} is destabilized by such smaller voids relative to its H-bonded isobutanal precursors. Tight confinement within voids that approach the dimensions of guest molecules brings forth entropic penalties and the need for distortions and atomic reorganizations in both the host and the guest; these are more consequential for the larger TS_{prins} than for H-bonded isobutanal (Section 3.4) and account for the smaller k_{prins}/K_{al} values in BEA and TON than in FAU.

Protons within MFI frameworks predominantly reside at cage-like channel intersections, where they act to give larger k_{prins}/K_{al} values than within straight BEA channels or their intersections (38 ± 1 vs. $15 \pm 4 \text{ ks}^{-1} \text{ kPa}^{-1}$ per H^+ , Fig. 7), in spite of the equivalent diameters for MFI and BEA void structures (0.70 vs. 0.67–0.69 nm, Table 1). DFT treatments indicate that MFI intersections provide more effective van der Waals stabilization for both the H-bonded isobutanal and TS_{prins} moieties than BEA channels; such trends are more consequential for TS_{prins} than for the smaller H-bonded isobutanal species, thus leading to larger k_{prins}/K_{al} values at MFI intersections than at BEA channels. These different k_{prins}/K_{al} values at MFI intersections and BEA channels illustrate how van der Waals interactions depend not only on the size, but also on the shape, of the confining voids, rendering spherical constructs

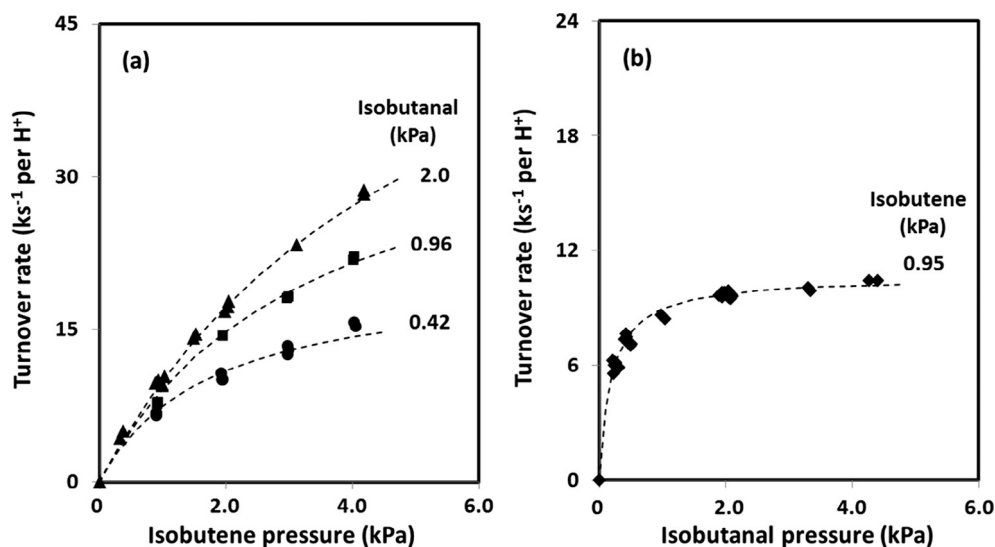
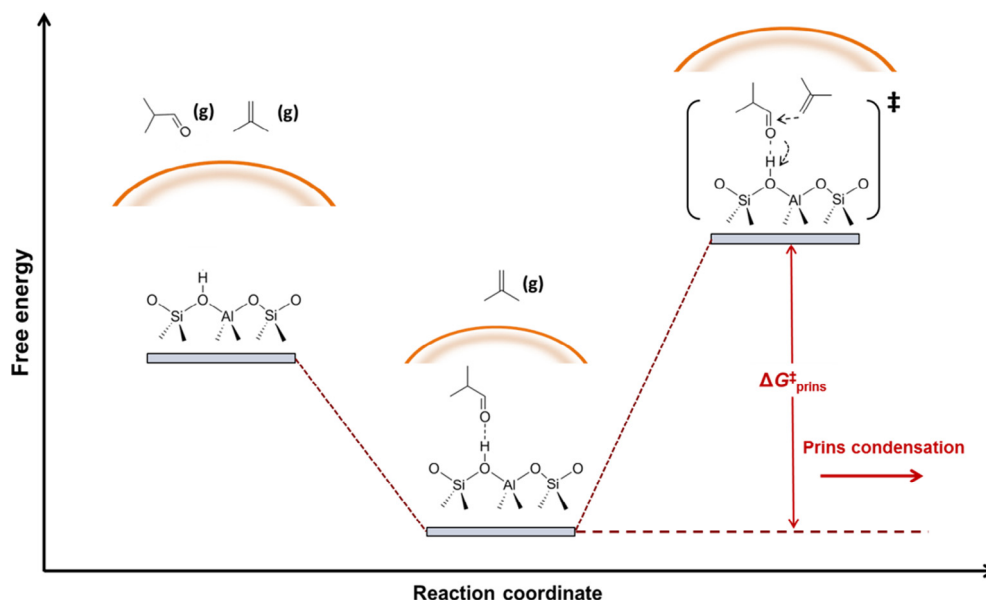


Fig. 6. Effects of (a) isobutene pressure and (b) isobutanal pressure on isobutanal–isobutene Prins condensation turnover rates (H-TON; 473 K; 0–4.5 kPa isobutanal; 0–4.5 kPa isobutene). Dashed curves represent regressed fits to the functional form of Eq. (10).



Scheme 4. Schematic reaction coordinate diagram for isobutanol-isobutene Prins condensation. $\Delta G_{\text{prins}}^{\ddagger}$ represents the experimentally-accessible free energy barrier for isobutanol-isobutene Prins condensation in microporous and mesoporous aluminosilicates (Eq. (11)).

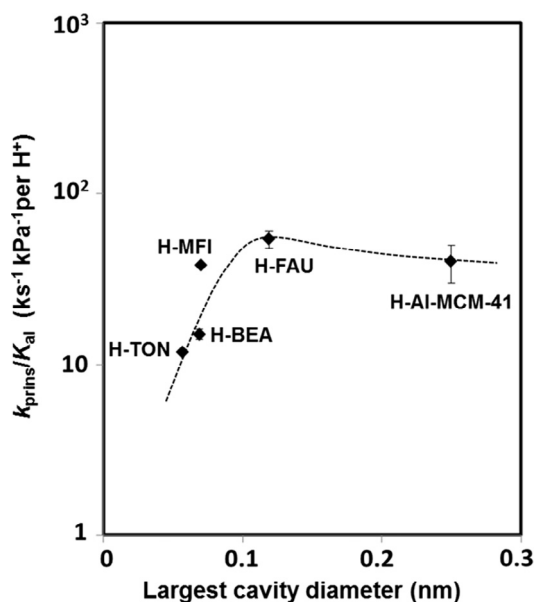


Fig. 7. Effects of void size on $k_{\text{prins}}/K_{\text{al}}$ values for isobutanol-isobutene Prins condensation on aluminosilicates at 473 K. The dashed line depicts a qualitative trend.

incomplete as descriptors of the effectiveness of confinement. A more appropriate treatment of host-guest interactions within confined spaces must rely on accurate assessments of geometries and energies for the relevant species and the confining voids, such as those provided by theoretical treatments that consider the van der Waals interactions consequential for the effects of confinement on stability of organic moieties and thus on their reactivity.

3.3. Theoretical treatments of adsorbed species in microporous aluminosilicate voids

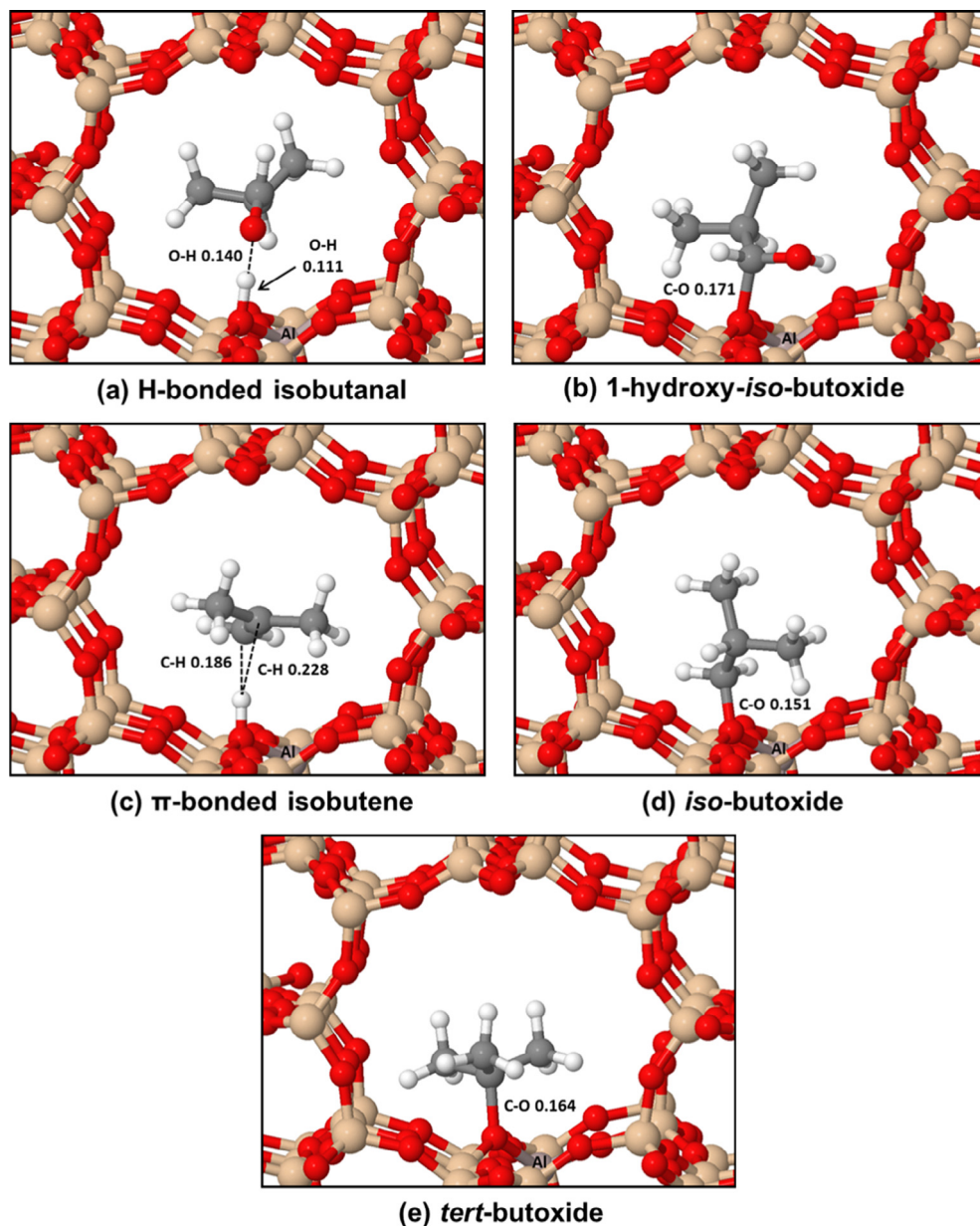
In this section, we describe the use of DFT methods that account for dispersive forces in accounting for the energies and structures of isobutanol and isobutene adsorbed at protons and of their respective adsorption equilibrium constants (K_{al} and K_{ene}) in order

to assess the stabilization that underpins confinement effects on Prins condensation rates (Eq. (7)).

Isobutanol forms a H-bond through its O-atom with a proton or abstracts the proton to form a 1-hydroxy-*iso*-butoxide attached to a framework O-anion via its carbonyl C-atom. Their DFT-derived structures are shown in Scheme 5 at the Al1–O1(H) location in the TON framework as illustrative examples. The distance between the O-atom in H-bonded isobutanol and the proton is 0.140 nm, and that of the proton from the framework O-atom (0.111 nm; Scheme 5a) is only slightly longer than this distance for the proton in the initial TON structure proton (0.098 nm), consistent with H-bonding. The distance between the α -C atom in 1-hydroxy-*iso*-butoxides and the framework O-atom is 0.171 nm (Scheme 5b); this distance is much shorter than the combined van der Waals radii of a C-atom and an O-atom (0.32 nm), in line with covalent attachment upon proton transfer [16].

Fig. 8 depicts adsorption free energies ($\langle \Delta G_{\text{ads}} \rangle$, Eq. (4)) and their enthalpy components ($\langle \Delta H_{\text{ads}} \rangle$) for H-bonded isobutanol and 1-hydroxy-*iso*-butoxide species ensemble-averaged over the four distinct proton locations for each Al T-site in TON, BEA, MFI, FAU, and Al-MCM-41 (473 K, 1 bar henceforth; ensemble-averaging described in Section 2.3; ΔG_{ads} and ΔH_{ads} values at each proton location in Table S2, SI); these values are referenced to the bare proton and a gaseous isobutanol at each location. The $\langle \Delta G_{\text{ads}} \rangle$ values for H-bonded isobutanol at each of the four TON T-sites range from -27 to -44 kJ mol^{-1} (Fig. 8a), while those for 1-hydroxy-*iso*-butoxide are positive ($+12$ to 31 kJ mol^{-1} ; Fig. 8a). These different $\langle \Delta G_{\text{ads}} \rangle$ values for the two adsorbed species reflect the predominant effects of the enthalpy differences between H-bonded isobutanals ($\langle \Delta H_{\text{ads}} \rangle$ -127 to -140 kJ mol^{-1} , Fig. 8b) and 1-hydroxy-*iso*-butoxides (-77 to -102 kJ mol^{-1} , Fig. 8b) at these temperatures.

The exponential means of the $\langle \Delta G_{\text{ads}} \rangle$ values over all T-sites in TON ($\langle \langle \Delta G_{\text{ads}} \rangle \rangle$, Eq. (5)) for H-bonded isobutanol and 1-hydroxy-*iso*-butoxide species are -41 and $+17$ kJ mol^{-1} (Table S3, SI), respectively, indicating that H-bonded isobutanol is the prevalent isobutanol-derived bound species. The resulting adsorption constant ($K_{\text{al}} = 3.4 \times 10^2$ kPa^{-1} , 473 K) is consistent with the near-saturation coverages of isobutanol-derived species prevalent even at very low isobutanol pressures (0.2–4.0 kPa; Section 3.1) and with the zero-order dependence of Prins condensation rates on isobutanol pressure on TON (Fig. 6b).



Scheme 5. DFT-optimized structures of adsorbed species formed from isobutanal ((a) H-bonded isobutanal and (b) 1-hydroxy-*iso*-butoxide) and isobutene ((c) π -bonded isobutene, (d) *iso*-butoxide, and (e) *tert*-butoxide) on proton sites in H-TON (Al1–O1(H) sites (Section 2.3); PBE + D3BJ). Distances are reported in nm.

A similar preference for H-bonded isobutanal over 1-hydroxy-*iso*-butoxide is evident on BEA (9 T-sites, $\langle\Delta G_{\text{ads}}\rangle$ -42 to -66 kJ mol^{-1} vs. $+40$ to $+11$ kJ mol^{-1} , Fig. 8c), MFI (12 T-sites, $\langle\Delta G_{\text{ads}}\rangle$ -23 to -88 kJ mol^{-1} vs. $+18$ to -31 kJ mol^{-1} , Fig. 8e), FAU (1 T-site, $\langle\Delta G_{\text{ads}}\rangle$ -47 kJ mol^{-1} vs. $+13$ kJ mol^{-1} , Fig. 8g), and Al-MCM-41 (1 T-site, $\langle\Delta G_{\text{ads}}\rangle$ -8 kJ mol^{-1} vs. $+20$ kJ mol^{-1} , Fig. 8g). The ranges of $\langle\Delta G_{\text{ads}}\rangle$ values among the 12 T-sites in MFI for H-bonded isobutanal (65 kJ mol^{-1}) and 1-hydroxy-*iso*-butoxide (49 kJ mol^{-1}) are much broader than for the 4 T-sites in TON (17 and 19 kJ mol^{-1}) and the 9 T-sites in BEA (24 and 29 kJ mol^{-1}), a reflection of the greater diversity of confining environments for the T-sites within MFI voids than in the other frameworks.

Isobutene can interact with protons to form π -bonded isobutenes, *iso*-butoxides, or *tert*-butoxides via C=C interactions with the proton or by transferring of proton to the bound species. The distances between the primary and tertiary C-atoms and the proton in the π -bonded isobutene at the Al1–O1(H) site in TON are

0.186 and 0.228 nm, respectively (Scheme 5c). *iso*-Butoxide and *tert*-butoxide species form covalent bonds with the O1-atom in TON (0.151 and 0.164 nm C–O bonds, respectively; Scheme 5d–e). The longer C–O distances in *tert*-butoxides (than for *iso*-butoxides) reflect the role of steric hindrance at the tertiary C-atom, caused by repulsion from framework O-atoms, which becomes particularly evident for the highly curved surfaces of the small channels in TON [16].

Fig. 9 depicts ensemble-averaged adsorption free energies ($\langle\Delta G_{\text{ads}}\rangle$) and the respective adsorption enthalpies ($\langle\Delta H_{\text{ads}}\rangle$) for π -bonded isobutenes, *iso*-butoxides, and *tert*-butoxides at each T-site in TON, BEA, MFI, FAU, and Al-MCM-41 (523 K, 1 bar) referenced to a bare proton site and a gaseous isobutene (ΔG_{ads} and ΔH_{ads} values for each proton location reported in Table S2, S1). On all T-sites in TON, *iso*-butoxides are more stable than *tert*-butoxides (the range of $\langle\Delta G_{\text{ads}}\rangle$ differences is -23 to -47 kJ mol^{-1} , Fig. 9a), but less stable than π -bonded isobutenes ($\langle\Delta G_{\text{ads}}\rangle$

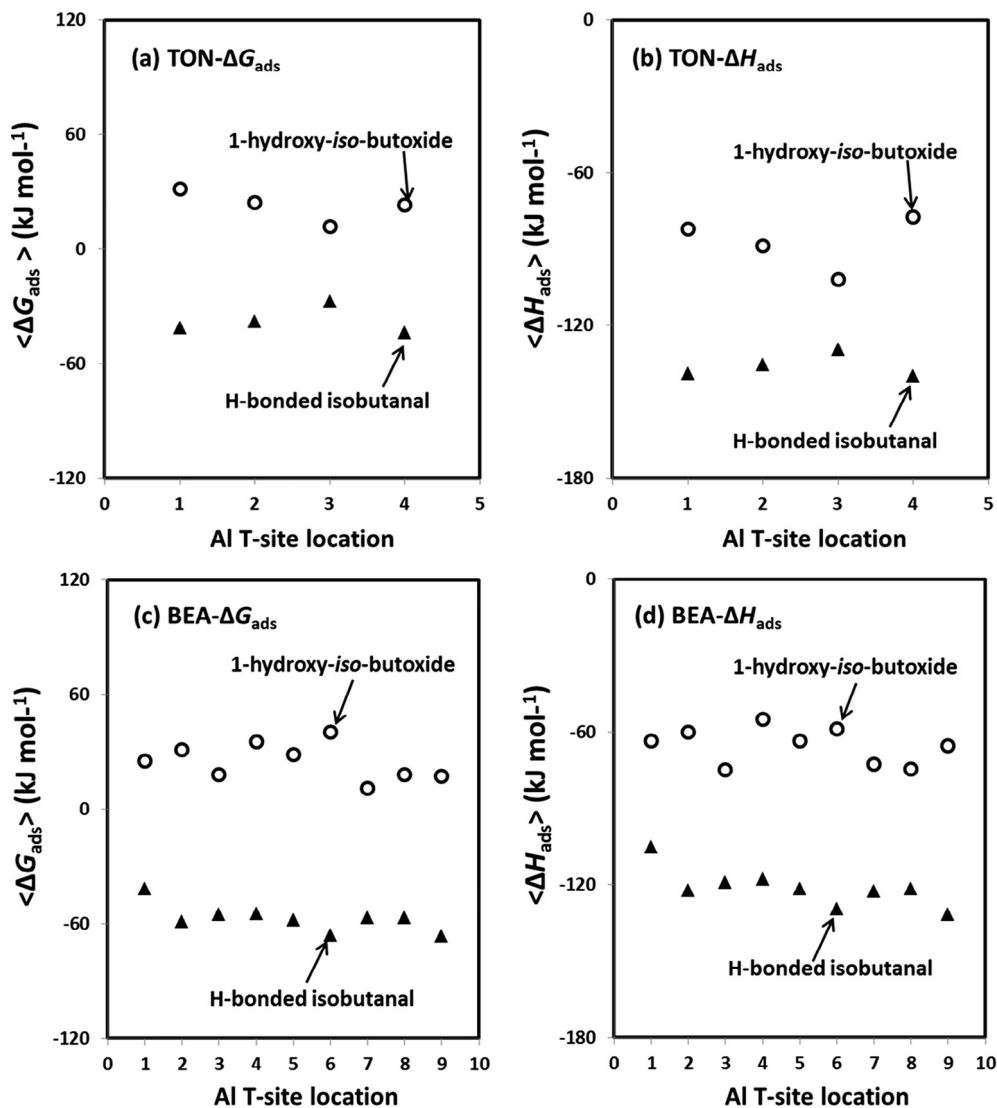


Fig. 8. DFT-derived ensemble-averaged adsorption free energies for H-bonded isobutanol (▲) and 1-hydroxy-iso-butoxide (○) species formed from isobutanol at proton sites in microporous and mesoporous aluminosilicates (PBE + D3BJ; 473 K, 1 bar isobutanol; relative to a bare proton site and a gaseous isobutanol molecule).

differences from -12 to -69 kJ mol^{-1} , Fig. 9a). This preference for the π -bonded structures seems inconsistent with the disappearance of zeolite O–H infrared bands upon contact with isobutene, which occurs without the concurrent appearance of perturbed O–H bands [16]. These apparent discrepancies may reflect the ubiquitous inaccuracies in entropy estimates from periodic DFT calculations, because DFT-derived enthalpies on most TONT-sites are in fact similar for π -bonded isobutenes and *iso*-butoxides (the range of $\langle \Delta H_{\text{ads}} \rangle$ difference: -13 to 3 kJ mol^{-1} for T1–T3 sites, Fig. 9b).

Similar DFT-derived stability differences among the possible forms of isobutene-derived bound species are evident for T-sites in BEA (Fig. 9c), MFI (Fig. 9e), and FAU (Fig. 9g). In contrast, *tert*-butoxides ($\Delta G_{\text{ads}} -10 \text{ kJ mol}^{-1}$, Fig. 9g) on Al-MCM-41 are slightly more stable than π -bonded isobutenes ($\Delta G_{\text{ads}} -4 \text{ kJ mol}^{-1}$) and *iso*-butoxides ($\Delta G_{\text{ads}} 0 \text{ kJ mol}^{-1}$), a consequence of the more negative ΔH_{ads} values for *tert*-butoxide (-81 kJ mol^{-1} , Fig. 9h) than for π -bonded isobutene (-61 kJ mol^{-1}) and *iso*-butoxide (-72 kJ mol^{-1}). The prevalence of *tert*-butoxides among isobutene-derived species on Al-MCM-41 reflects the absence of steric hindrance at the tertiary C-atom upon formation of the covalent C–O bond on aluminosilicate surfaces that are much less curved than on the smaller voids in zeolites [5].

The measured adsorption constants K_m ($m = \text{al}$ for isobutanol; $m = \text{ene}$ for isobutene; Eq. (7)) for each framework depend on the free energies ($\langle \Delta G_{\text{ads}} \rangle_m$) ensemble-averaged over all bound configurations [16]:

$$K_m = \exp\left(-\frac{\langle \Delta G_{\text{ads}} \rangle_m}{k_B T}\right) \quad (13)$$

$$\exp\left(-\frac{\langle \Delta G_{\text{ads}} \rangle_m}{k_B T}\right) = \sum_n \exp\left(-\frac{\langle \Delta G_{\text{ads}} \rangle_{m,n}}{k_B T}\right) \quad (14)$$

in which $\langle \Delta G_{\text{ads}} \rangle_{m,n}$ is the $\langle \Delta G_{\text{ads}} \rangle$ value (Eq. (5)) for the n th configuration formed from isobutanol (H-bonded isobutanol or 1-hydroxy-*iso*-butoxide) or from isobutene (π -bonded isobutene, *iso*-butoxide, or *tert*-butoxide). DFT-derived $\langle \Delta G_{\text{ads}} \rangle$ values for these bound species, averaged over all T-site locations in TON, MFI, BEA, FAU, and Al-MCM-41 and for T-site locations in the channel interactions of MFI (T1 and T5–T12 sites), are listed in Table S3 (SI). For all bound configurations derived from isobutanol and isobutene in MFI, the $\langle \Delta G_{\text{ads}} \rangle$ values were slightly less negative by $\sim 1 \text{ kJ mol}^{-1}$ (473 K, 1 bar) than when averaged only over T-sites located at channel

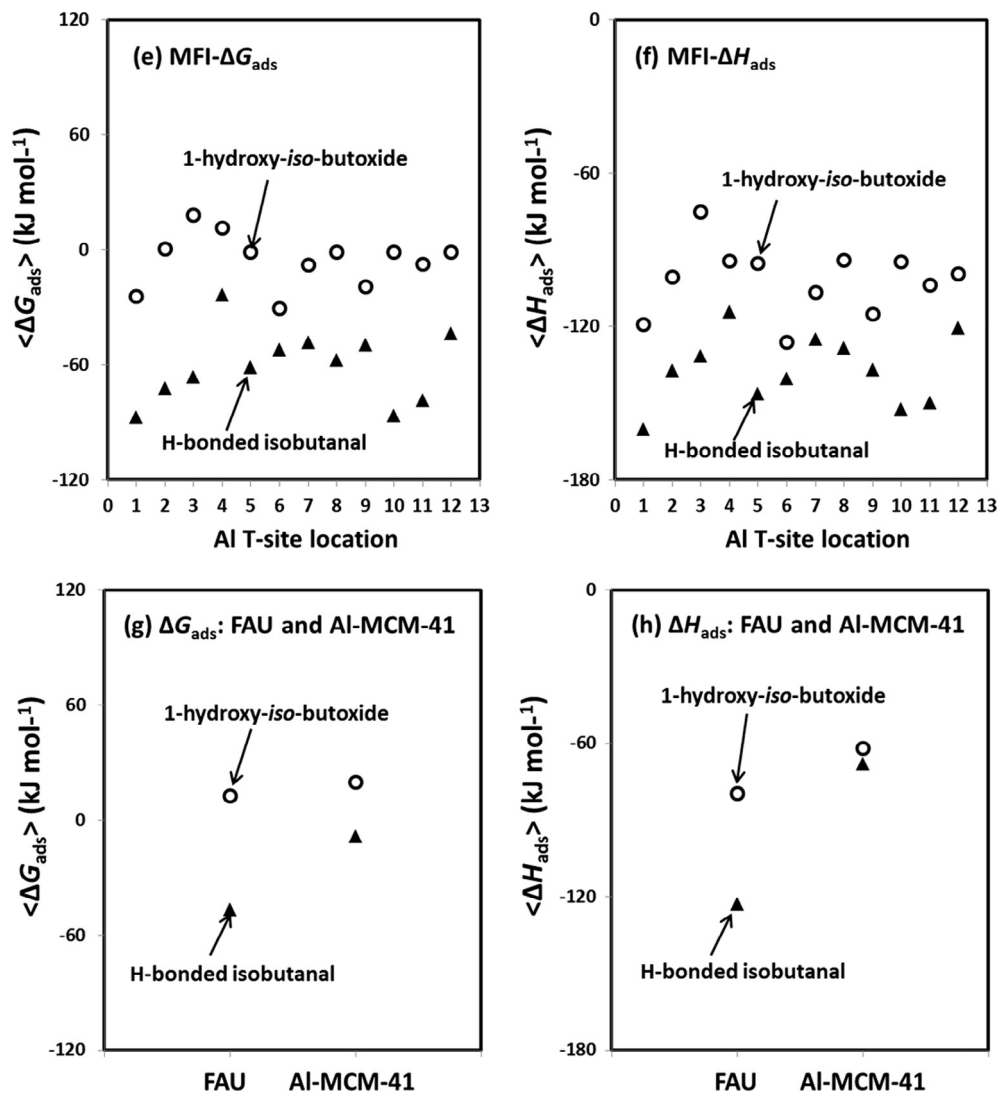


Fig. 8 (continued)

interactions (Table S3, SI), indicating that protons within MFI channels and channel intersections stabilize these C₄ bound species to the same extent, making measured $\langle \Delta G_{\text{ads}} \rangle$ values (Eq. (13)) insensitive to the specific location of Al sites among intersection T-sites. In contrast, DFT treatments show that TS_{prins} structures are more stable within channels than at their intersections (Section 3.4). Measured $\Delta G_{\text{prins}}^{\ddagger}$ values and mean values for Al sites only at intersections illustrate the predominant presence of protons at intersections at these Si/Al ratios (Si/Al = 16.6–43.8; Section 3.4), as previously found from kinetic and DFT assessments of elimination reactions on the same MFI samples [22].

Fig. 10a shows $\langle \Delta G_{\text{ads}} \rangle_{\text{al}}$ and $\langle \Delta G_{\text{ads}} \rangle_{\text{ene}}$ values that become more negative with decreasing void size (MCM-41, FAU, MFI, and BEA), but which reverse this trend for the smaller voids in TON, leading to optimal stability for both bound species for voids of ~0.7 nm diameter; these dimensions resemble those along the long axes in these bound species (0.71 nm isobutanol; 0.68 nm isobutene). The $\langle \Delta G_{\text{ads}} \rangle_{\text{al}}$ values are more negative than for $\langle \Delta G_{\text{ads}} \rangle_{\text{ene}}$ (by 18–43 kJ mol⁻¹, 473 K and 1 bar, Fig. 10a) for both smaller (0.57 nm; TON) and larger (1.19 nm; FAU) voids. Such free energy differences between $\langle \Delta G_{\text{ads}} \rangle_{\text{al}}$ and $\langle \Delta G_{\text{ads}} \rangle_{\text{ene}}$ lead to higher coverages of isobutanol than isobutene (by 10–5600 factors for isobutanol/isobutene

ratios of 0.1) on all samples, as also evident from Prins condensation rates (Section 3.1).

The attractive van der Waals components (ΔG_{vdw}) of adsorption free energies (ΔG_{ads}) are estimated here using two-body interaction potentials implemented in D3BJ functionals [40]. Specifically, ΔG_{vdw} values are given by the sum of all two-body dispersion interaction energies between each atom in the organic moiety and each atom in the aluminosilicate framework at their respective location in their optimized structures. As in the case of Equation (3), ensemble-averages of such ΔG_{vdw} values for bound species over all four proton locations at each Al T-site ($\langle \Delta G_{\text{vdw}} \rangle$) are given by

$$\langle \Delta G_{\text{vdw}} \rangle = \frac{\sum_{i=1}^4 \left[\Delta G_{\text{vdw},i} \exp\left(\frac{-G_{\text{guest},i}}{k_B T}\right) \right]}{\sum_{i=1}^4 \exp\left(\frac{-G_{\text{guest},i}}{k_B T}\right)} \quad (15)$$

where $G_{\text{guest},i}$ is the free energy for the bound species at the proton (or O-atom) location i , and $\Delta G_{\text{vdw},i}$ is the total dispersive interaction energy for the bound species at each location i .

The ensemble averages of these $\langle \Delta G_{\text{vdw}} \rangle$ components ($\langle \langle \Delta G_{\text{vdw}} \rangle \rangle$) over all T-site locations for TON, BEA, FAU, and Al-MCM-41 and over T-site locations at channel intersections in MFI were

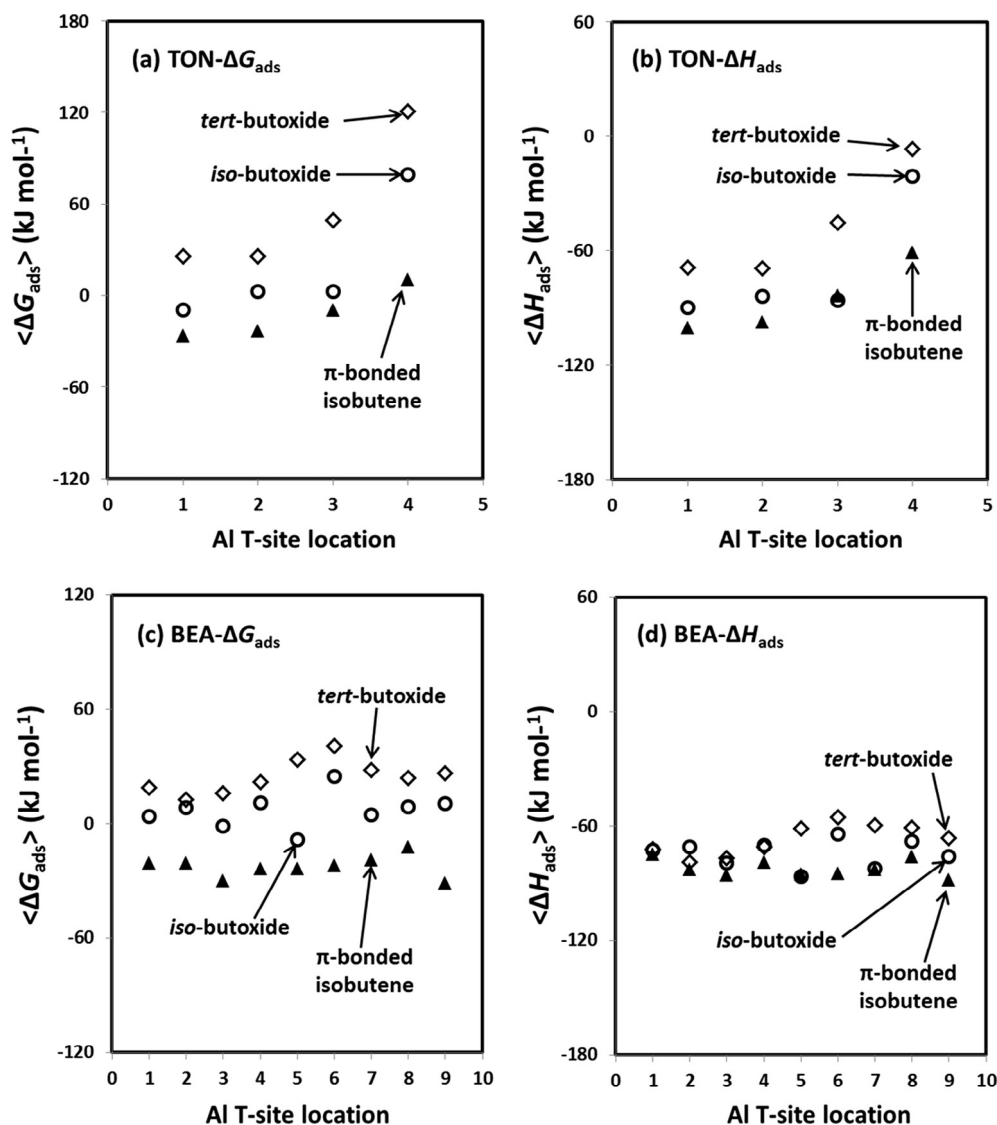


Fig. 9. DFT-derived ensemble-averaged adsorption free energies for π -bonded isobutene (▲), *iso*-butoxide (○), and *tert*-butoxide (◇) species formed from isobutene at proton sites in microporous and mesoporous aluminosilicates (PBE + D3BJ); 473 K, 1 bar isobutene; relative to a bare proton site and a gaseous isobutene molecule.

calculated as in the case of $\overline{\langle \Delta G_{\text{ads}} \rangle}$ (Eq. (5)), but with the $\langle \Delta G_{\text{ads}} \rangle$ term in Equation (5) replaced by $\langle \Delta G_{\text{vdw}} \rangle$. The $\langle \Delta G_{\text{vdw}} \rangle$ values for H-bonded isobutanol and π -bonded isobutene differ in energy by less than 11 kJ mol⁻¹ among all frameworks (Fig. 10b), consistent with the similar sizes of these two bound species and with their similar ability to establish van der Waals contacts with void walls. For both species, $\langle \Delta G_{\text{vdw}} \rangle$ values become more negative with decreasing void size (Fig. 10b), because of their more effective contacts with such voids. $\langle \Delta G_{\text{vdw}} \rangle$ values at MFI intersections are more negative than within BEA channels (H-bonded isobutanol -82 vs. -53 kJ mol⁻¹; π -bonded isobutene -74 vs. -56 kJ mol⁻¹, Fig. 10b), in spite of their similar sizes, an indication of the more effective confinement of these structures within the quasi-spherical MFI cages than in the cylinder-like BEA structures; these $\langle \Delta G_{\text{vdw}} \rangle$ differences between MFI and BEA were also observed for alkoxides derived from isobutanol and isobutene (Table S3, SI). Van der Waals interactions become stronger as the size of the confining voids decreases, even on TON, for which the total free energy of all bound species is, in fact, higher than in larger voids (Fig. 10a). The latter reflects the distortions of bound species and framework atoms (atomic displacements in TON caused for effective van der

Waals contacts with H-bonded isobutanol shown in Fig. S2 (SI) as an illustrative example); these distortions incur enthalpic and entropic penalties and become more evident for tighter host-guest configurations (Section 3.4).

$\langle \Delta G_{\text{vdw}} \rangle$ values provide an accurate measure of the van der Waals contributions to the stability of all bound species (transition states and intermediates), but such values, by themselves, remain incomplete descriptors of reactivity, because the structural distortions of the host-guest system and entropy losses of guest species upon confinement differ between transition states and their relevant precursors, as we discuss next in the context of transition state theory formalisms and density functional theory calculations.

3.4. Theoretical treatments of confinement effects on Prins condensation reactivity

Measured $k_{\text{prins}}/K_{\text{al}}$ values (Table 3) reflect the free energy differences ($\Delta G_{\text{prins}}^\ddagger$; Eqs. (11) and (12)) between TS_{prins} structures ($G_{\text{prins}}^\ddagger$) and one H-bonded isobutanol (G_{als}) and one gaseous isobutene (G_{ene}). Here we use a Born-Haber thermochemical cycle

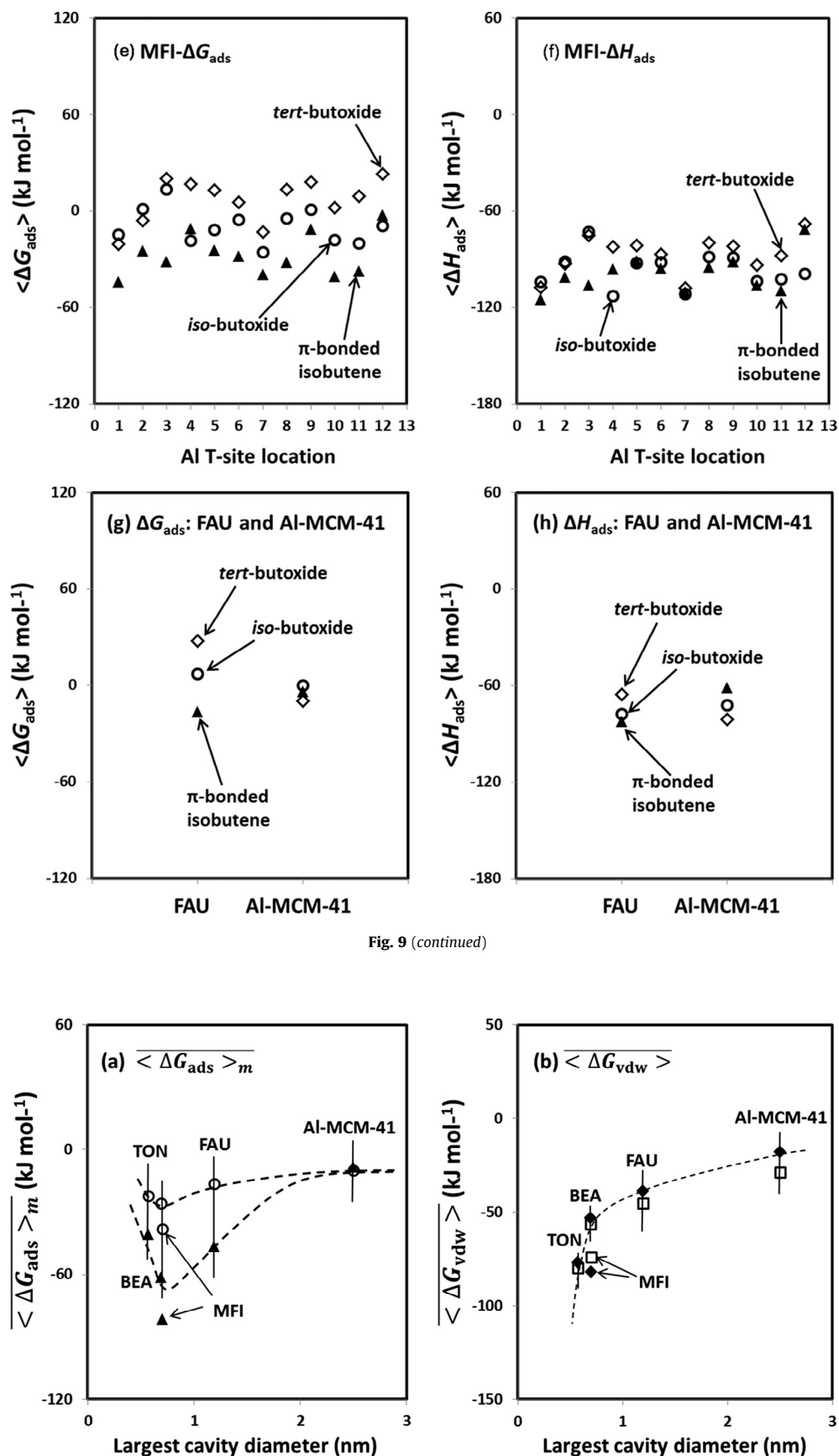


Fig. 9 (continued)

Fig. 10. DFT-derived (a) ensemble-averaged $\overline{\langle \Delta G_{ads} \rangle}_m$ values for adsorption of isobutanal ($m = al$; \blacktriangledown) and isobutene ($m = ene$; \circ) at protons on aluminosilicates and (b) the corresponding $\overline{\langle \Delta G_{vdw} \rangle}$ components for H-bonded isobutanal (\blacklozenge) and π -bonded isobutene (\square) configurations (PBE + D3BJ; 473 K, 1 bar; relative to a bare proton site and a gaseous isobutanol or isobutene molecule). The energies for TON, BEA, FAU, and Al-MCM-41 represent ensemble-averages over all T-site locations; the energies for MFI are ensemble-averages over all T-site locations at MFI intersections. Dashed lines indicate quantitative trends.

(depicted in Scheme 6) in order to dissect the relevant contributions of confinement to reactivity.

The difference in free energies of a given bound moiety between their confined and unconfined states ($\Delta G_{\text{confine}}^X$; $X = \text{TS}$ (for the Prins TS structures); al (for H-bonded isobutanals); Scheme 6) is as follows:

$$\Delta G_{\text{confine}}^X = \Delta G_{\text{vdw}}^X + \Delta G_{\text{distortion}}^X + \Delta G_{\text{entropy}}^X \quad (16)$$

with ΔG_{vdw}^X and $\Delta G_{\text{distortion}}^X$ representing the components of $\Delta G_{\text{confine}}^X$ from the attractive van der Waals interactions and the host-guest structural distortions upon confining the organic moiety, respectively; $\Delta G_{\text{entropy}}^X$ is the separate component of $\Delta G_{\text{confine}}^X$ due to entropy losses upon confinement.

In the thermochemical cycle of Scheme 6, the difference between $\Delta G_{\text{confine}}^{\text{TS}}$ and $\Delta G_{\text{confine}}^{\text{al}}$ ($\Delta \Delta G_{\text{confine}}^{\text{TS-al}}$) equals that between the confined and unconfined TS_{prins} structures ($\Delta G_{\text{prins}}^\ddagger$ and $\Delta G_{\text{prins,u}}^\ddagger$, respectively):

$$\Delta \Delta G_{\text{confine}}^{\text{TS-al}} = \Delta G_{\text{prins}}^\ddagger - \Delta G_{\text{prins,u}}^\ddagger \quad (17)$$

which accounts for the confinement consequences for Prins condensation reactivity. Combining Equations (16) and (17) then gives

$$\Delta \Delta G_{\text{confine}}^{\text{TS-al}} = \Delta G_{\text{vdw}}^{\text{TS}} + \Delta G_{\text{distortion}}^{\text{TS}} + \Delta G_{\text{entropy}}^{\text{TS}} - \Delta G_{\text{vdw}}^{\text{al}} - \Delta G_{\text{distortion}}^{\text{al}} - \Delta G_{\text{entropy}}^{\text{al}} \quad (18)$$

and allows confinement effects to be dissected into three free energy components:

$$\Delta \Delta G_{\text{confine}}^{\text{TS-al}} = \Delta \Delta G_{\text{vdw}}^{\text{TS-al}} + \Delta \Delta G_{\text{distortion}}^{\text{TS-al}} + \Delta \Delta G_{\text{entropy}}^{\text{TS-al}} \quad (19)$$

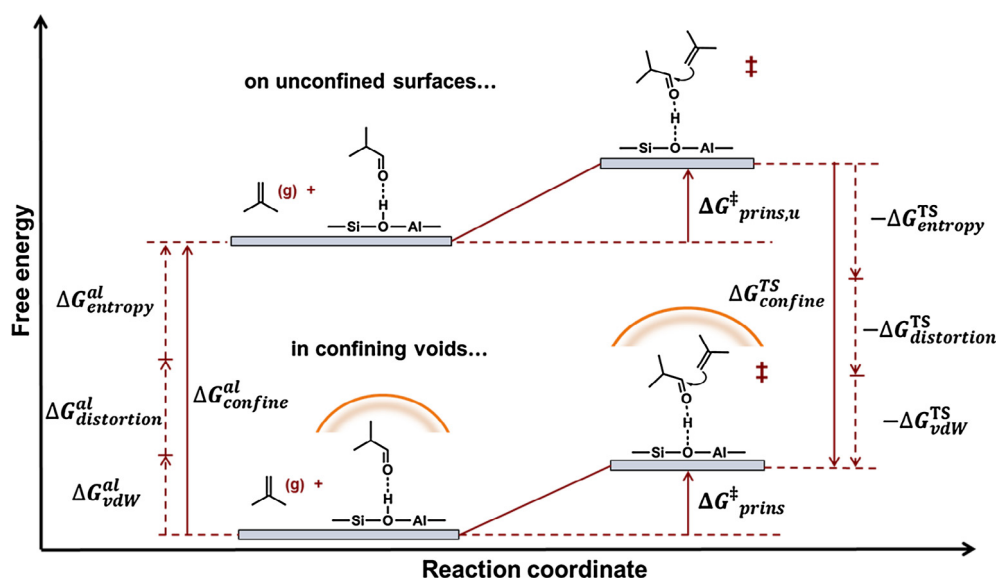
$\Delta \Delta G_{\text{vdw}}^{\text{TS-al}}$, $\Delta \Delta G_{\text{distortion}}^{\text{TS-al}}$, and $\Delta \Delta G_{\text{entropy}}^{\text{TS-al}}$ are the respective ΔG_{vdw}^X , $\Delta G_{\text{distortion}}^X$, and $\Delta G_{\text{entropy}}^X$ differences between TS_{prins} and its relevant H-bonded isobutanal precursor.

We choose here the 4-hydroxy-2,5-dimethyl-hexan-2-ylum C_8 carbenium ion (Scheme 7; the product formed from the C–C coupling TS) as a proxy for TS_{prins} in order to avoid the need to optimize TS_{prins} at each T-site in each framework. This C_8 carbenium

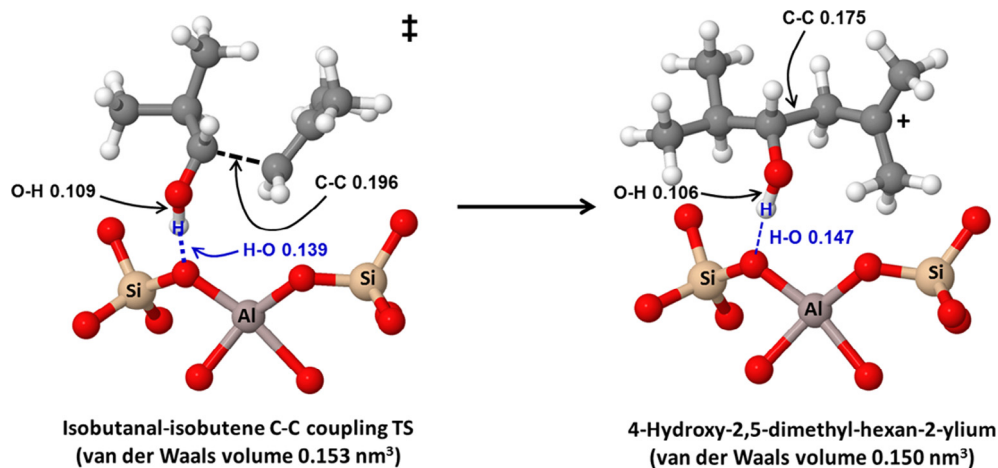
ion is similar in size and shape to TS_{prins} (0.531 vs. 0.535 nm on Al-MCM-41 [5]), because of the lateness of TS_{prins} and thus represents an accurate surrogate for how TS_{prins} structures interact with the surrounding voids. The size and shape of this C_8 carbenium ion is insensitive to the nature of the aluminosilicate framework (0.528–0.534 nm for TON, BEA, MFI, FAU, and Al-MCM-41).

These $\Delta \Delta G_{\text{vdw}}^{\text{TS-al}}$ values (Eq. (19)) are given by the difference between ΔG_{vdw} values for bound 4-hydroxy-2,5-dimethyl-hexan-2-ylum ions and H-bonded isobutanal species estimated at each site in each framework using D3BJ functionals. Averaging $\Delta \Delta G_{\text{vdw}}^{\text{TS-al}}$ over the four distinct O-atoms at each Al T-site ($\langle \Delta \Delta G_{\text{vdw}}^{\text{TS-al}} \rangle$) and then over all Al T-sites in each framework ($\overline{\langle \Delta \Delta G_{\text{vdw}}^{\text{TS-al}} \rangle}$) was done as in the case of bound intermediates ($\langle \Delta G_{\text{vdw}} \rangle$, Eq. (15); $\overline{\langle \Delta G_{\text{vdw}} \rangle}$, Eq. (5); Section 3.3), also assuming uniform Al siting among all T-sites in TON, BEA, FAU, and Al-MCM-41 and among all intersection T-sites in MFI. These protocols were also used to average $\Delta \Delta G_{\text{distortion}}^{\text{TS-al}}$ and $\Delta \Delta G_{\text{entropy}}^{\text{TS-al}}$ over all accessible Al T-sites, but replacing the ΔG_{vdw} values by the respective $\Delta G_{\text{distortion}}$ and $\Delta G_{\text{entropy}}$ values.

Fig. 11a shows $\langle \Delta \Delta G_{\text{vdw}}^{\text{TS-al}} \rangle$ values for each aluminosilicate framework as a function of the void size (473 K, 1 bar; values for Al-MCM-41 set as the energy reference; $\Delta \Delta G_{\text{vdw}}^{\text{TS-al}}$ values for each proton site in each framework shown in Table S4, SI). These $\langle \Delta \Delta G_{\text{vdw}}^{\text{TS-al}} \rangle$ values become more negative (–15 to –42 kJ mol^{–1}, Fig. 11a) as the void size decreases from FAU, BEA, to TON, indicating that van der Waals forces preferentially stabilize TS_{prins} structures over their smaller H-bonded isobutanal precursors. The values of $\langle \Delta \Delta G_{\text{vdw}}^{\text{TS-al}} \rangle$ at MFI intersections are more negative (by 30 kJ mol^{–1}) than within BEA channels of similar size (Fig. 11a), indicating a preferential benefit of the cage-like structures at MFI intersections over the cylinder-like BEA channels for $\langle \Delta \Delta G_{\text{vdw}}^{\text{TS-al}} \rangle$; such $\langle \Delta \Delta G_{\text{vdw}}^{\text{TS-al}} \rangle$ differences illustrate the significant effects of



Scheme 6. Thermochemical cycle describing measured free energy barriers for Prins condensation at protons located within confining aluminosilicate frameworks ($\Delta G_{\text{prins}}^\ddagger$) in terms of the respective free energy barriers on unconfined aluminosilicates ($\Delta G_{\text{prins,u}}^\ddagger$) and the free energy changes for H-bonded isobutanals ($\Delta G_{\text{confine}}^{\text{al}}$) and Prins condensation transition states ($\Delta G_{\text{confine}}^{\text{TS}}$) conferred by confinement (with respect to the free energies on unconfined aluminosilicate surfaces). These $\Delta G_{\text{confine}}^X$ terms ($X = \text{al}$ or TS) can be decomposed into the sum of ΔG_{vdw}^X , $\Delta G_{\text{distortion}}^X$, and $\Delta G_{\text{entropy}}^X$, which reflect the contributions of van der Waals interaction of the bound species with the confining framework, the structural distortions of the bound species and the framework, and the entropy losses of the bound species upon confinement, respectively, to $\Delta G_{\text{confine}}^X$ values.



Scheme 7. DFT-derived structures for the isobutanol-isobutene Prins condensation C–C coupling transition state and the C₈ carbenium ion product formed from this transition state on aluminosilicate surfaces (PBE + D3BJ). Distances are reported in nm. The C–C coupling transition state structure is adapted from [5].

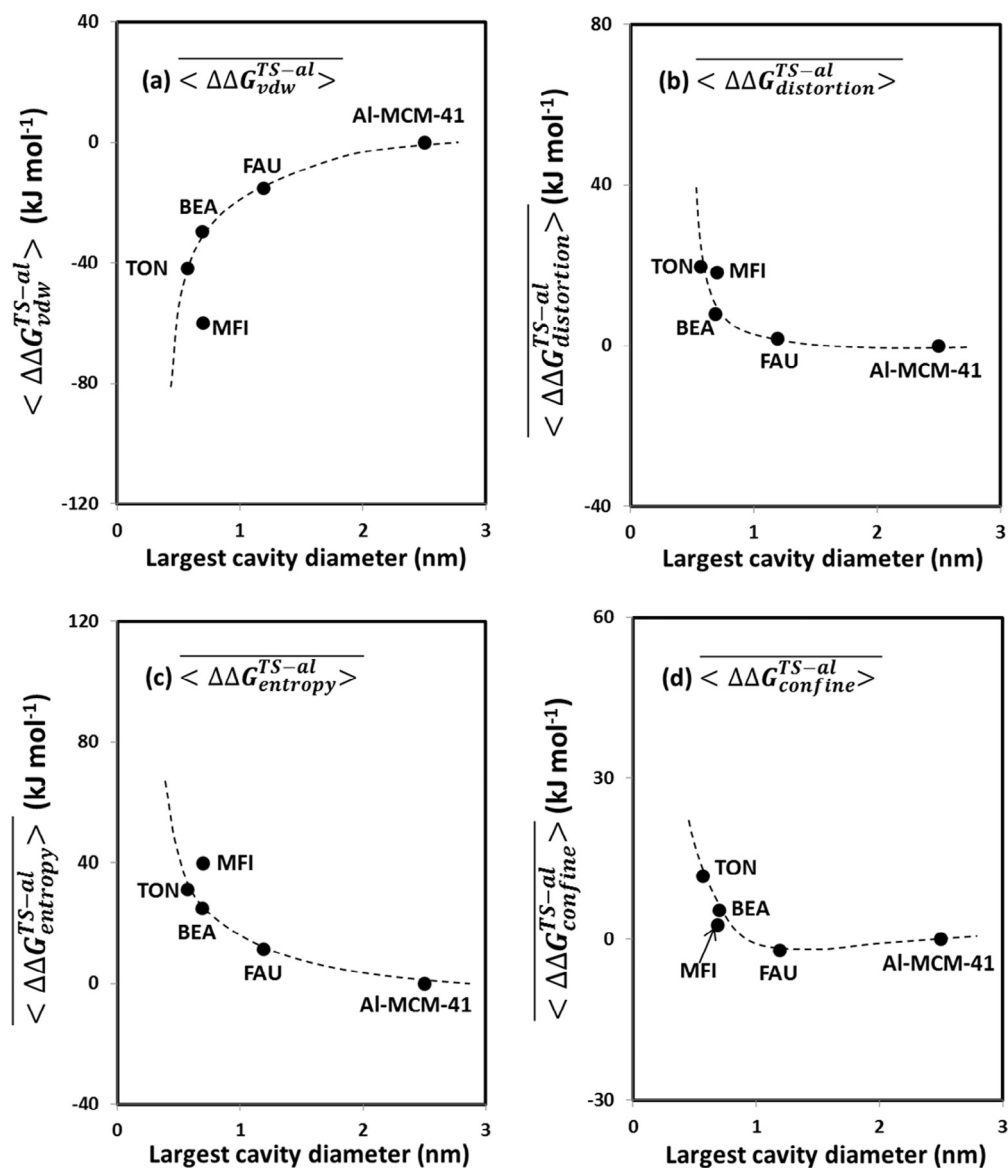


Fig. 11. DFT-derived ensemble-averaged $\langle \Delta \Delta G_{vdw}^{TS-al} \rangle$, $\langle \Delta \Delta G_{distortion}^{TS-al} \rangle$, $\langle \Delta \Delta G_{entropy}^{TS-al} \rangle$ and $\langle \Delta \Delta G_{confine}^{TS-al} \rangle$ values as a function of the void size (PBE + D3BJ; 473 K, 1 bar; the values for unconfined aluminosilicate surfaces (Al-MCM-41) chosen as energy references). The energies for TON, BEA, FAU, and Al-MCM-41 were ensemble-averaged over all T-site locations; the energies for MFI were ensemble-averaged over T-site locations of the MFI intersections. Dash lines indicate quantitative trends.

shape in accounting for van der Waals contacts and the incomplete nature of size descriptors based on spherical constructs.

The $\Delta G_{\text{distortion}}$ values were determined from the combined electronic energies for the organic moiety (E_{guest}) and the inorganic framework moiety (E_{ZH}) relative to their fully relaxed structures when both reside at mutually non-interacting distances (E_{guest}^* ; E_{ZH}^*):

$$\Delta G_{\text{distortion}} = E_{\text{guest}} - E_{\text{guest}}^* + E_{\text{ZH}} - E_{\text{ZH}}^* \quad (20)$$

The difference between $\Delta G_{\text{distortion}}$ values for bound 4-hydroxy-2,5-dimethyl-hexan-2-ylum ions and H-bonded isobutanal species was used to estimate the $\Delta\Delta G_{\text{distortion}}^{\text{TS-al}}$ component in overall $\Delta\Delta G_{\text{confine}}^{\text{TS-al}}$ values (Eq. (19)). DFT-derived $\Delta\Delta G_{\text{distortion}}^{\text{TS-al}}$ values at each proton site in each framework are all positive (Table S4, SI), reflecting the larger distortion (and consequently larger energy penalties) for TS_{prins} than for the smaller H-bonded isobutanal species.

Ensemble-averaged $\langle\Delta\Delta G_{\text{distortion}}^{\text{TS-al}}\rangle$ values increase from 2 to 20 kJ mol^{-1} as void size decreases from FAU, BEA, to TON (Al-MCM-41 is used as the energy reference; Fig. 11b), also consistent with distortions of the silicate framework and the organic moiety that are more consequential for TS_{prins} than for its smaller H-bonded isobutanal precursor. This trend in $\langle\Delta\Delta G_{\text{distortion}}^{\text{TS-al}}\rangle$ values with void size is opposite to that for $\langle\Delta\Delta G_{\text{vdw}}^{\text{TS-al}}\rangle$ values (Fig. 11a), reflecting distortions provide the required geometry for effective host-guest van der Waals contacts [16]. $\langle\Delta\Delta G_{\text{distortion}}^{\text{TS-al}}\rangle$ values at quasi-spherical MFI intersections are larger than within cylinder-like BEA channels (18 vs. 8 kJ mol^{-1} , Fig. 11b); they are compensated by more negative $\langle\Delta\Delta G_{\text{vdw}}^{\text{TS-al}}\rangle$ values, because such distortions mediate a better fit between the organic moieties and the inorganic framework.

The $\Delta G_{\text{entropy}}$ components in $\Delta G_{\text{confine}}$ values are given by

$$\Delta G_{\text{entropy}} = T(S_{\text{guest}} - S_{\text{guest}}^*) \quad (21)$$

Here, S_{guest} is the entropy of the bound organic moiety in a given framework and S_{guest}^* is its entropy on Al-MCM-41. As in the case of $\Delta\Delta G_{\text{distortion}}^{\text{TS-al}}$, $\Delta\Delta G_{\text{entropy}}^{\text{TS-al}}$ values at each proton site in each framework are positive (Table S4, SI), indicative of larger entropy losses upon confinement for TS_{prins} than for H-bonded isobutanal. Ensemble-averaged $\langle\Delta\Delta G_{\text{entropy}}^{\text{TS-al}}\rangle$ values (relative to Al-MCM-41 bound species) depend on the size and shape of the aluminosilicate voids and vary within 11–40 kJ mol^{-1} (473 K, 1 bar, Fig. 11c) among FAU, MFI, BEA, and TON, resembling the corresponding $\langle\Delta\Delta G_{\text{distortion}}^{\text{TS-al}}\rangle$ values in trend (Fig. 11b). These similar effects of confinement on $\langle\Delta\Delta G_{\text{entropy}}^{\text{TS-al}}\rangle$ and $\langle\Delta\Delta G_{\text{distortion}}^{\text{TS-al}}\rangle$ reflect the concomitance of entropy losses and structural distortions brought forth by confining TS_{prins} and its H-bonded isobutanal precursor within molecule-size voids.

The sum of $\Delta\Delta G_{\text{vdw}}^{\text{TS-al}}$, $\Delta\Delta G_{\text{distortion}}^{\text{TS-al}}$, and $\Delta\Delta G_{\text{entropy}}^{\text{TS-al}}$ gives $\Delta\Delta G_{\text{confine}}^{\text{TS-al}}$ (Eq. (19)), the free energy descriptor of the magnitude of confinement effects on Prins condensation reactivity (Scheme 6). $\langle\Delta\Delta G_{\text{confine}}^{\text{TS-al}}\rangle$ values averaged over all T-site locations for TON, BEA, FAU, and Al-MCM-41 and over all T-site intersection locations for MFI are shown in Fig. 11d (473 K, 1 bar; data for Al-MCM-41 set as the free energy reference). The negative $\langle\Delta\Delta G_{\text{confine}}^{\text{TS-al}}\rangle$ values for FAU (-2 kJ mol^{-1} , relative to Al-MCM-41, Fig. 11d) indicate that FAU frameworks are more effective than Al-MCM-41 channels in

preferentially stabilizing TS_{prins} over H-bonded isobutanal through van der Waals contacts, leading to higher Prins condensation turnover rates.

$\langle\Delta\Delta G_{\text{confine}}^{\text{TS-al}}\rangle$ values become positive and larger as voids become smaller than those of FAU (1.19 nm; -2 kJ mol^{-1} , Fig. 11d). These positive values for BEA (0.69 nm; $+3 \text{ kJ mol}^{-1}$) and TON (0.57 nm; $+9 \text{ kJ mol}^{-1}$) indicate that structural distortions and entropy losses destabilize TS_{prins} in these smaller voids, leading to highest rates within voids of intermediate size. MFI intersections gave negative $\langle\Delta\Delta G_{\text{confine}}^{\text{TS-al}}\rangle$ values relative to Al-MCM-41, again in contrast with the positive values observed for BEA channels similar in size (-2 vs. $+3 \text{ kJ mol}^{-1}$, Fig. 11d). These trends in DFT-derived $\langle\Delta\Delta G_{\text{confine}}^{\text{TS-al}}\rangle$ values agree well with those obtained from measured $k_{\text{prins}}/K_{\text{al}}$ values (Fig. 7), as shown by the linear relation evident in the semi-logarithmic plot in Fig. 12, confirming that $\langle\Delta\Delta G_{\text{confine}}^{\text{TS-al}}\rangle$ values represent realistic descriptions of the effects of confinement on the stability of TS_{prins} and its H-bonded isobutanal precursor.

$\langle\Delta\Delta G_{\text{confine}}^{\text{TS-al}}\rangle$ values averaged over all T-site locations in MFI are more negative than those only over T-site locations in MFI intersections (-8 vs. -2 kJ mol^{-1} , Fig. 12; open and filled data points), reflecting the different confinement environments at MFI channels and their intersections (void size: 0.50 vs. 0.70 nm, Table 1). $\langle\Delta\Delta G_{\text{confine}}^{\text{TS-al}}\rangle$ values at MFI intersections lie along the trend line shown in Fig. 12 between DFT-derived $\langle\Delta\Delta G_{\text{confine}}^{\text{TS-al}}\rangle$ and measure $k_{\text{prins}}/K_{\text{al}}$ values for TON, FAU, BEA, and Al-MCM-41 (Fig. 12), but those averaged over all MFI Al T-sites do not, suggesting that Al sites and the associated protons reside predominantly at channel intersection in these MFI samples.

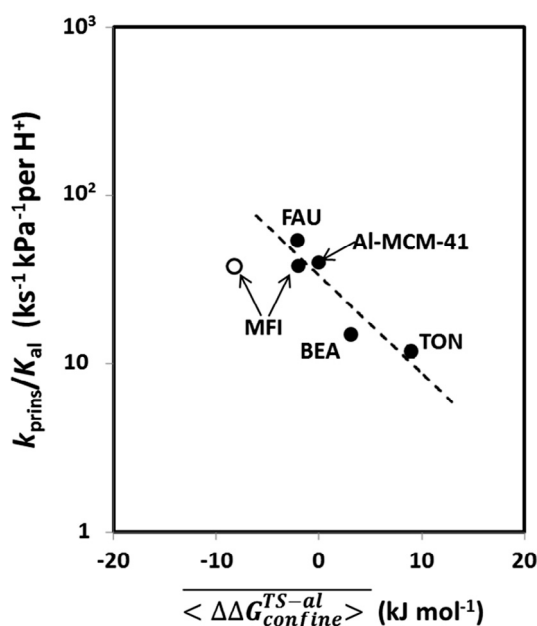
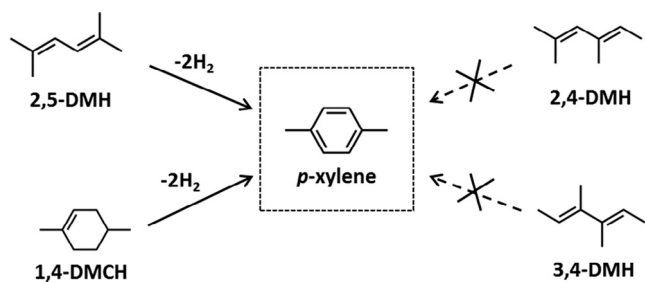


Fig. 12. Correlation between DFT-derived $\langle\Delta\Delta G_{\text{confine}}^{\text{TS-al}}\rangle$ and measured Prins condensation rate constant $k_{\text{prins}}/K_{\text{al}}$ for aluminosilicate frameworks (PBE + D3BJ; 473 K, 1 bar; $k_{\text{prins}}/K_{\text{al}}$ data from Fig. 7). The energies for TON, BEA, FAU, and Al-MCM-41 were ensemble-averaged over all T-site locations (●); the energies for MFI were ensemble-averaged over T-site locations of the MFI intersections (●) and also over all T-site locations in MFI (○). The dashed line represents an exponential regression fit for the data labeled by (●).



Scheme 8. Formations of *p*-xylene from 2,5-dimethyl-hexadiene (2,5-DMH) and 1,4-dimethyl-cyclohexene (1,4-DMCH). 2,4-DMH and 3,4-DMH are not right precursors to *p*-xylene.

3.5. Confinement effects on the secondary interconversion of primary isobutanol-isobutene Prins condensation products

The skeletal isomers of primary 2,5-DMH products (e.g. 2,4-DMH and 3,4-DMH) cannot directly form *p*-xylene (Scheme 8), while 2,5-DMH and its 1,4-DMCH cyclization product are direct precursors to such arenes via dehydrocyclization and dehydrogenation reactions [6,7], respectively (Scheme 8). The selectivities to these secondary products of 2,5-DMH diene isomers on aluminosilicates are reported here as a function of reactant conversion, varied through changes in reactor residence time, in order to probe the relative rates of primary and secondary reaction routes and

their sensitivity to confinement effects conferred by the voids within aluminosilicate solid acids (2.0 kPa isobutanol, 1.0 kPa isobutene, 473 K).

The selectivities to isomerization and cyclization products of 2,5-DMH interconversions both increased with increasing residence time and reactant conversion on all aluminosilicates (FAU, BEA, MFI, and TON in Fig. 13 and Al-MCM-41 [5]). 2,5-DMH predominantly converts to skeletal diene isomers on FAU, BEA, and TON with isomer selectivities of 13%, 28%, 10%, respectively, at the same isobutene conversion (10%) and with much lower selectivity to cycloalkenes (3–5%; Fig. 13a–c). The higher selectivities to skeletal and cyclic isomers on BEA channels relative to the larger FAU cages and the smaller TON channels indicate that isomerization TS structures are stabilized more effectively by van der Waals contacts relative to the TS structures that mediate Prins condensation turnovers within voids of intermediate size. As a result, high selectivities to primary 2,5-DMH products are preferred on aluminosilicates with smaller or larger confining spaces than those prevalent in BEA zeolite frameworks.

The cage-like structures prevalent at MFI channel intersections give a much higher selectivity to cyclic 1,4-DMCH alkene regioisomers than cylindrical BEA channels of similar effective diameter (Fig. 13b and d; 36% vs. 5% at 10% isobutene conversion), while confining voids in MFI and BEA give similar selectivities to skeletal isomers (28–29%). The uniquely high selectivity to cyclic 1,4-DMCH regioisomers on MFI is insensitive to their proton density (2.1–3.6 H⁺ per unit cell, Fig. S3, SI); such constant selectivities,

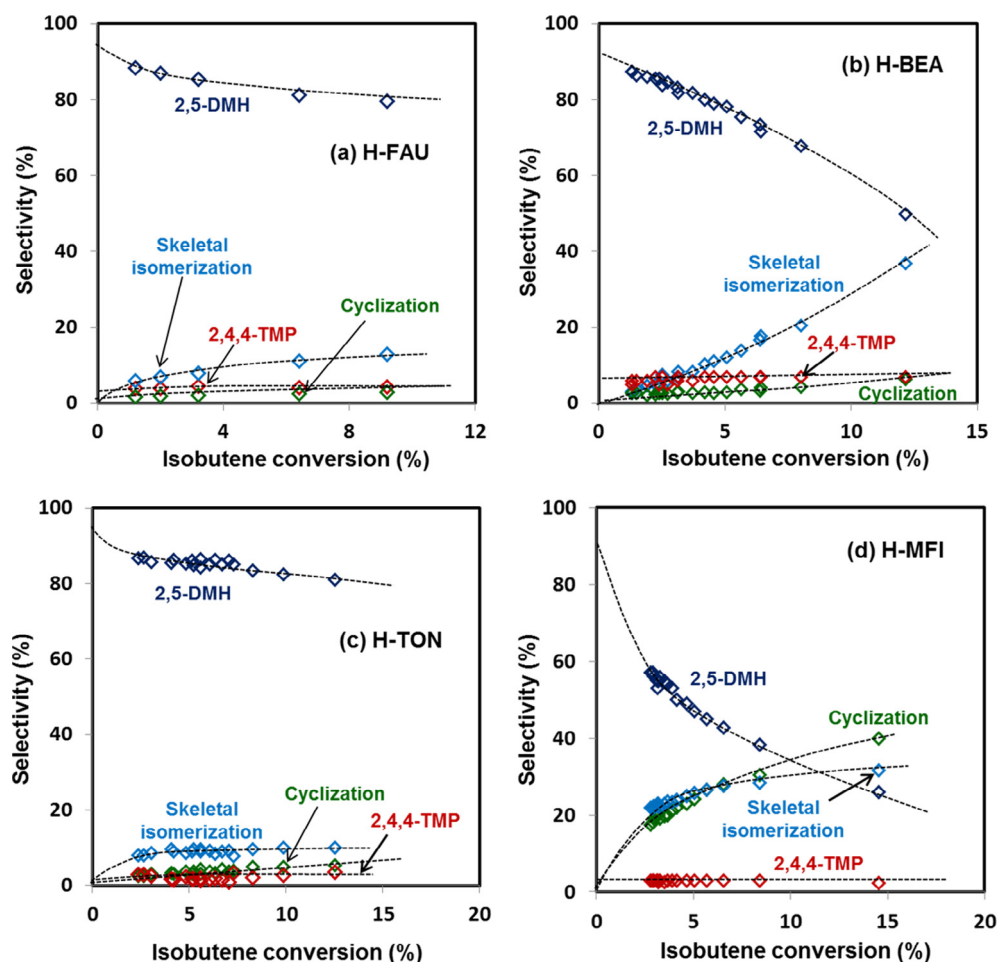


Fig. 13. Selectivities of 2,5-DMH and respective skeletal and cyclic isomers and 2,4,4-TMP as a function of isobutene conversion on (a) H-FAU, (b) H-BEA, (c) H-TON, and (d) H-MFI (473 K; 2.0 kPa isobutanol; 1.0 kPa isobutene). Dashed curves indicate quantitative trends.

Table 4
Arithmetically-averaged molecular length and width for Prins condensation products.^a

Molecule	Length (nm)	Width (nm)
2,5-DMH	1.00	0.66
1,4-DMCH	0.94	0.68
2,4-DMH	1.01	0.69
3,4-DMH	1.00	0.71

^a Gaussian 09, DSD-PBEP86-D3BJ/Def2-TZVP; optimized configurations for each molecule and their sizes shown in Fig. S5, SI.

taking together with the constant Prins condensation turnover rates on MFI samples with different proton densities (Fig. S4, SI), preclude any enhancement of such secondary reactions by diffusional constraints to the intracrystalline removal of primary 2,5-DMH products caused by the cage-like undulations along MFI channels. The high cyclization/isomerization selectivity ratios on MFI (with respect to BEA; 1.2 vs. 0.18; 10% isobutene conversion) thus reflect cyclization TS structures that are preferentially stabilized within such void structures relative to isomerization TS structures. These strong effects of local void shape on TS stability illustrate once again the incomplete nature of descriptors that treat the complex topologies within crystalline aluminosilicates using dimensions obtained from circumscribing quasi-spherical volumes, and which cannot account for van der Waals contacts that depend sensitively also on the detailed geometries of the inorganic hosts and of the bound organic moieties within them [16,28].

DFT-derived molecular length and width of 1,4-DMCH are 0.94 and 0.68 nm, respectively (Table 4); both of them are smaller than those of 2,4-DMH and 3,4-DMH (1.00–1.01 nm length and 0.69–0.71 nm width). These size differences between the cyclic and skeletal isomers of 2,5-DMH suggest that cyclization TS structures would also be smaller than for isomerization, based on the product-like nature of the transition states that mediate these acid-catalyzed reactions [51,52]. Therefore, the higher cyclization/isomerization selectivity ratios on MFI than BEA imply preferential stabilization of smaller guests in MFI channel intersections than in BEA channels of similar diameter, consistent with the “dimpled” surfaces of the cage-like voids formed by the interconnecting channels within MFI frameworks.

4. Conclusions

Isobutanol-isobutene Prins condensation on protons of microporous and mesoporous aluminosilicates is kinetically limited by the C–C bond formation of H-bonded isobutanol with a gaseous isobutene, whereas the concurrent isobutene oligomerization is kinetically limited by the C–C bond formation of isobutene-derived alkoxide species with the same gaseous isobutene. The similar sizes of the C–C bond formation transition states that mediate these reactions lead to insignificant dependence of the selectivities to these reactions on the size and shape of aluminosilicate voids and thus to analogous consequences of confinement on their individual reactivity.

Measured Prins condensation rate constants reflect differences between the free energy for the C–C bond formation transition state and those for its H-bonded isobutanol precursor, the most abundant surface species on protons at catalytic conditions, and a gaseous isobutene. These rate constants are higher for FAU than larger voids (Al-MCM-41), because of the less effective van der Waals contacts of the larger voids with the transition state (with respect to H-bonded isobutanol), and also smaller voids (TON, BEA, and MFI), because of energy penalties brought forth by the structural distortions of the aluminosilicate framework and the organic moiety and concomitant entropy losses of the latter upon

confinement by the smaller voids. Quasi-spherical MFI intersections, where protons reside in MFI, show higher rate constants than cylinder-like BEA channels of similar size, reflecting the shape of confining voids also affects the effectiveness of van der Waals stabilization for bound species.

The secondary skeletal isomerization and cyclization reactions of 2,5-DMH Prins condensation products are favored at higher conversion and voids of intermediate size (BEA and MFI), which stabilize their kinetically-relevant transition states more effectively than for the Prins condensation C–C bond formation transition states. MFI frameworks show a unique high selectivity to the cyclic 1,4-dimethyl-cyclohexene product, indicative of preferential stabilization of the cyclization transition states over the larger isomerization transition states conferred by the “dimpled” surfaces of the MFI intersections.

Acknowledgments

The research reported here was supported as part of the BP Conversion Consortium (BP-XC²) at the University of California at Berkeley. The authors gratefully acknowledge Drs. Eric Dskocil, John Shabaker, Glenn Sunley, and other members of the XC² program members at BP p.l.c. and Drs. Stanley Herrmann, Michele Sarazen, and David Hibbitts at UC Berkeley for their technical suggestions during the course of this study, and also Dr. Yongchun Hong (UC Berkeley) for the careful review of this manuscript. Computational facilities were provided by the Extreme Science and Engineering Discovery Environment (XSEDE), which is supported by National Science Foundation (grant number ACI-1548562).

Appendix A. Supplementary material

Supplementary data associated with this article can be found, in the online version, at <http://dx.doi.org/10.1016/j.jcat.2017.06.012>.

References

- [1] T. Yamaguchi, C. Nishimichi, *Catal. Today* 16 (1993) 555–562.
- [2] T.J. Taylor, J.D. Taylor, M.W. Peters, D.E. Henton, US Patent 8 742 187 B2 (2014), to GEVO, Inc.
- [3] H. Wang, Z. Liu, C. Sun, G. Wang, *Catal. Today* 93–95 (2004) 425–431.
- [4] H. Wang, Z. Liu, C. Sun, G. Wang, *Catal. Commun.* 5 (2004) 41–43.
- [5] S. Wang, E. Iglesia, *ACS Catal.* 6 (2016) 7664–7684.
- [6] E. Iglesia, J.E. Baumgartner, *Stud. Surf. Sci. Catal.* 75 (1993) 993–1006.
- [7] X. Feng, T.H. Colle, G.D. Mohr, US Patent 6653518, B2 (2003), to ExxonMobil Chemical Patents Inc.
- [8] P.P. Peralta-Yahya, F. Zhang, S.B. del Cardayre, J.D. Keasling, *Nature* 448 (2012) 320–328.
- [9] M.J.L. Gines, E. Iglesia, *J. Catal.* 176 (1998) 155–172.
- [10] M. Xu, M.J.L. Gines, A. Hilmen, B.L. Stephens, E. Iglesia, *J. Catal.* 171 (1997) 130–147.
- [11] E.I. Gürbüz, D.D. Hibbitts, E. Iglesia, *J. Am. Chem. Soc.* 137 (2015) 11984–11985.
- [12] J. Macht, M.J. Janik, M. Neurock, E. Iglesia, *J. Am. Chem. Soc.* 130 (2008) 10369–10379.
- [13] W. Knaeble, R.T. Carr, E. Iglesia, *J. Catal.* 319 (2014) 283–296.
- [14] F. Leydier, C. Chizallet, D. Costa, P. Raybaud, *J. Catal.* 325 (2015) 35–47.
- [15] M.L. Sarazen, E. Dskocil, E. Iglesia, *ACS Catal.* 6 (2016) 7059–7070.
- [16] M.L. Sarazen, E. Dskocil, E. Iglesia, *J. Catal.* 344 (2016) 553–569.
- [17] S. Abate, K. Barbera, G. Centi, P. Lanzafame, S. Perathoner, *Catal. Sci. Technol.* 6 (2016) 2485–2501.
- [18] R. Gounder, A.J. Jones, R.T. Carr, E. Iglesia, *J. Catal.* 286 (2012) 214–223.
- [19] R. Gounder, E. Iglesia, *Chem. Commun.* 49 (2013) 3491–3509.
- [20] E.G. Derouane, *J. Catal.* 100 (1986) 541–544.
- [21] G. Sastre, A. Corma, *J. Mol. Catal. A* 305 (2009) 3–7.
- [22] A.J. Jones, R.T. Carr, S.I. Zones, E. Iglesia, *J. Catal.* 312 (2014) 58–68.
- [23] A.J. Jones, S.I. Zones, E. Iglesia, *J. Phys. Chem. C* 118 (2014) 17787–17800.
- [24] H.Y. Luo, J.D. Lewis, Y. Román-Leshkov, *Annu. Rev. Chem. Biomol. Eng.* 7 (2016) 663–692.
- [25] P. Deshlahra, R.T. Carr, E. Iglesia, *J. Am. Chem. Soc.* 136 (2014) 15229–15247.
- [26] A.J. Jones, E. Iglesia, *ACS Catal.* 5 (2015) 5741–5755.
- [27] A. Ghorbanpour, J.D. Rimer, L.C. Grabow, *ACS Catal.* 6 (2016) 2287–2298.
- [28] S. Herrmann, E. Iglesia, *J. Catal.* 346 (2017) 134–153.

- [29] W.J. Ball, S.A.I. Barri, D. Young, EP 0104800 B1 (1986), to The British Petroleum Company p.l.c.
- [30] E.L. First, C.E. Gounaris, J. Wei, C.A. Floudas, *Phys. Chem. Chem. Phys.* 13 (2011) 17339–17358.
- [31] G. Kresse, J. Furthmuller, *J. Comput. Mater. Sci.* 6 (1996) 15–50.
- [32] G. Kresse, J. Furthmuller, *Phys. Rev. B* 54 (1996) 11169–11186.
- [33] G. Kresse, J. Hafner, *Phys. Rev. B* 47 (1993) 558–561.
- [34] G. Kresse, J. Hafner, *Phys. Rev. B* 49 (1994) 14251–14269.
- [35] J.P. Perdew, K. Burke, M. Ernzerhof, *Phys. Rev. Lett.* 77 (1996) 3865–3868.
- [36] J.P. Perdew, K. Burke, M. Ernzerhof, *Phys. Rev. Lett.* 78 (1997), 1396–1396.
- [37] P.E. Blochl, *Phys. Rev. B* 50 (1994) 17953–17979.
- [38] G. Kresse, D. Joubert, *Phys. Rev. B* 59 (1999) 1758–1775.
- [39] X. Wu, M.C. Vargas, S. Nayak, V. Lotrich, G. Scoles, *J. Chem. Phys.* 115 (2001) 8748–8757.
- [40] S. Grimme, S. Ehrlich, L. Goerigk, *J. Comp. Chem.* 32 (2011) 1456–1465.
- [41] D.A. McQuirrie, *Statistical Mechanics*, University Science Books, Sausalito, CA, 2000.
- [42] P. Deshlahra, E. Iglesia, *J. Phys. Chem. C* 118 (2014) 26115–26129.
- [43] C. Baerlocher, L.B. McCusker, *Database of Zeolite Structures*. <<http://www.iza-structure.org/databases/>> (accessed August 23, 2016).
- [44] A. Vjunov, J.L. Fulton, T. Huthwelker, S. Pin, D. Mei, G.K. Schenter, N. Govind, D. M. Camaioni, J.Z. Hu, J.A. Lercher, *J. Am. Chem. Soc.* 136 (2014) 8296–8306.
- [45] T. Yokoi, H. Mochizuki, S. Namba, J.N. Kondo, T. Tatsumi, *J. Phys. Chem. C* 119 (2015) 15303–15315.
- [46] N. Mehio, S. Dai, D. Jiang, *J. Phys. Chem. A* 118 (2014) 1150–1154.
- [47] X. Li, M.J. Frisch, *J. Chem. Theory Comput.* 2 (2006) 835–839.
- [48] S. Kozuch, J.M.L. Martin, *Phys. Chem. Chem. Phys.* 13 (2011) 20104–20107.
- [49] F. Weigend, R. Ahlrichs, *Phys. Chem. Chem. Phys.* 7 (2005) 3297–3305.
- [50] M.J. Frisch, G.W. Trucks, H.B. Schlegel, G.E. Scuseria, M.A. Robb, J.R. Cheeseman, G. Scalmani, V. Barone, B. Mennucci, G.A. Petersson, H. Nakatsuji, M. Caricato, X. Li, H. P. Hratchian, A. F. Izmaylov, J. Bloino, G. Zheng, J.L. Sonnenberg, M. Hada, M. Ehara, K. Toyota, R. Fukuda, J. Hasegawa, M. Ishida, T. Nakajima, Y. Honda, O. Kitao, H. Nakai, T. Vreven, J. Montgomery, Jr., J.E. Peralta, F. Ogliaro, M. Bearpark, J.J. Heyd, E. Brothers, K.N. Kudin, V.N. Staroverov, T. Keith, R. Kobayashi, J. Normand, K. Raghavachari, A. Rendell, J.C. Burant, S.S. Iyengar, J. Tomasi, M. Cossi, N. Rega, N.J. Millam, M. Klene, J.E. Knox, J. B. Cross, V. Bakken, C. Adamo, J. Jaramillo, R. Gomperts, R.E. Stratmann, O. Yazyev, A.J. Austin, R. Cammi, C. Pomelli, J.W. Ochterski, R.L. Martin, K. Morokuma, V.G. Zakrzewski, G.A. Voth, P. Salvador, J.J. Dannenberg, S. Dapprich, A.D. Daniels, Ö. Farkas, J.B. Foresman, J.V. Ortiz, J. Cioslowski, D.J. Fox, Gaussian 09, Rev. D.01, Gaussian Inc, Wallingford CT, 2013.
- [51] M.A. Natal-Santiago, R. Alcalá, J.A. Dumesic, *J. Catal.* 181 (1999) 124–144.
- [52] Y.V. Joshi, K.T. Thomson, *J. Catal.* 230 (2005) 440–463.